



# 1 Glacial-interglacial shifts in dominant climate forcing over the last 33 2 ka in the northern South China Sea

3 Xueqin Zhao<sup>\*, 1</sup>, Shengjie Ye<sup>1</sup>, Jiahui Yao<sup>1</sup>, Michael E. Meadows<sup>2, 3</sup>, Chengyu Weng<sup>4</sup>, Yasong Wang<sup>1</sup>,  
4 Mingxing Zhang<sup>1</sup>, Yunping Xu<sup>1</sup>

5 <sup>1</sup>Shanghai Frontiers Research Center of the Hadal Biosphere, College of Oceanography and Ecological Science, Shanghai  
6 Ocean University, Shanghai 201306, China

7 <sup>2</sup>School of Geography and Ocean Sciences, Nanjing University, Nanjing 210023, China

8 <sup>3</sup>Department of Environmental & Geographical Science, University of Cape Town, Cape Town 7701, South Africa

9 <sup>4</sup>State Key Laboratory of Marine Geology, Tongji University, Shanghai, China

10 *Correspondence to:* Xueqin Zhao (xqzhao@shou.edu.cn)

11 **Abstract.** The northern South China Sea is a critical region for understanding East Asian Monsoon dynamics. However,  
12 integrated, multi-proxy records elucidating long-term climatic and vegetation changes in this region remain fragmented, with  
13 a notable scarcity of coherent land-ocean interaction data during the Last Glacial Maximum (LGM). This gap has impeded  
14 progress in elucidating the mechanisms underpinning monsoon variability and in rigorously evaluating the performance of  
15 palaeoclimate models. To address this, we conducted a multi-proxy analysis combining palynological, organic- and inorganic-  
16 geochemical methods on a marine sediment core from the northern South China Sea to reconstruct environmental and oceanic  
17 dynamics at millennial-scale resolution that spans the last 33 ka. Our results reveal a clear contrast between glacial and  
18 interglacial conditions and drivers: the glacial period was characterized by higher sedimentation rates, elevated marine primary  
19 productivity, cooler climate, lower humidity and herb-dominated vegetation associated with enhanced fire activity in the  
20 adjacent terrestrial ecosystems. Deglaciation was characterized by pronounced warming and reduced productivity, together  
21 with increased moisture availability, a shift toward pine-dominated vegetation, minimal fire activity, and reduced fluvial input  
22 as the coastline retreated. The overall findings highlight a fundamental transition in climatic controls, from a regime dominated  
23 by sea level forcing during the glacial period to one increasingly governed by tropical ocean-atmosphere interactions initiated  
24 by early ocean warming during the interglacial.

## 25 1 Introduction

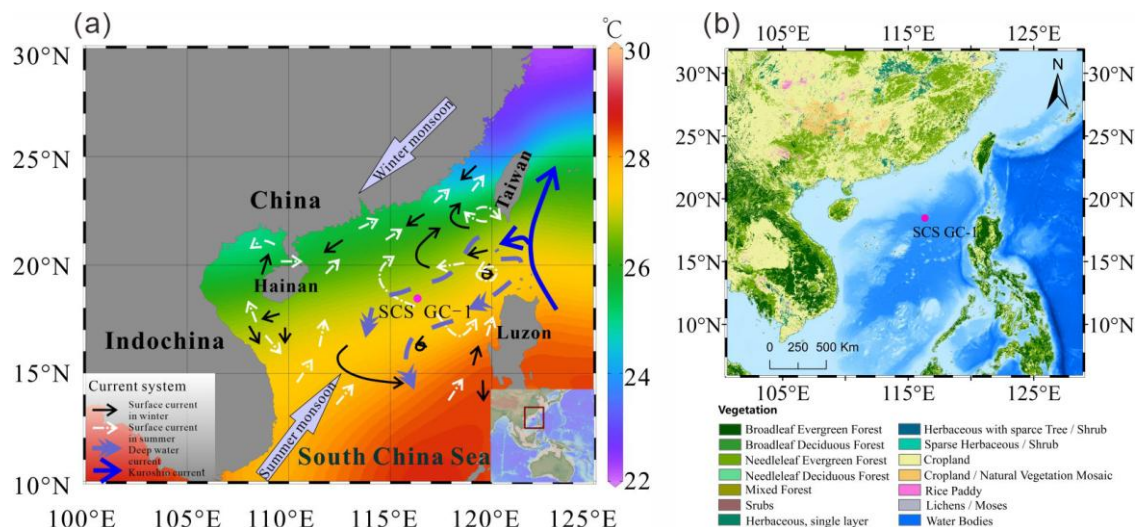
26 Low latitude regions play a critical role in the global climate and its dynamic because they are the seat of the most active  
27 moisture and heat exchanges between the atmosphere and the ocean expressed via the monsoon regime. Tropical and  
28 subtropical monsoon regions such as East Asia and the South China Sea (SCS) experience the most significant seasonal  
29 reversal in wind directions with associated migration of regional intense precipitation (Wang et al., 2017). Monsoon wind and  
30 precipitation patterns have changed significantly in the late Quaternary, influenced by gradual changes in insolation and  
31 internal interactions among the atmosphere, oceans, land surfaces and Northern Hemisphere ice sheets (An, 2000; Ding et al.,  
32 1994; Kissel et al., 2020; Tian et al., 2010; Wang et al., 2001). These changes have affected the climate and land-ocean energy  
33 balance of western Pacific marginal basins, whereas the influence and dynamics of the monsoon system remain insufficiently  
34 constrained. Investigations of paleoclimate variability have significant value in providing valuable insights into monsoonal  
35 dynamics across tectonic, orbital and millennial time scales.

36 Given the importance of the climate signature during the last Glacial Maximum (LGM, spanning approximately 26.5-19 ka)  
37 to climate model validation and testing, new reconstructions of precipitation and vegetation response during the LGM are  
38 necessary to resolve inconsistencies and improve model reliability. Marine sediments potentially record the interplay of the  
39 East Asian Monsoon, surface and deep oceanic circulation and sea level compared with other terrestrial records (Tian et al.,  
40 2004; Wang et al., 1999). The South China Sea is divided into a northern deep basin with isolated, oxygen-poor waters and a



41 southern extensive shelf province, a dichotomy fundamentally controlled by a ~2400 m deep sill that restricts deep-water  
42 exchange with the open Pacific (Chen and Huang, 1996). Due to its well-preserved sedimentary strata, abundant sediment  
43 supply, and relatively high sedimentation rates, the northern SCS is recognized as a key area with strong potential for high-  
44 resolution paleoenvironmental reconstructions. Such records can substantially enhance our ability to resolve global and  
45 regional climate variability during the Quaternary (Wang et al., 2014). A range of different proxies is preserved in marine  
46 sedimentary archives. Pollen evidence, for example, can provide a valuable signal of vegetation evolution on the adjacent  
47 continental land mass (Cheng et al., 2023; Luo et al., 2016; Sun et al., 2000a), while microcharcoal particles are widely used  
48 in palaeofire reconstruction to infer fire frequency, intensity and vegetation changes, and terrestrial ecosystem response  
49 (Conedera et al., 2009). Foraminifera are sensitive to environmental changes, and are widely applied as a paleo-proxy of marine  
50 conditions (Haynes, 1981), although the shells of planktonic foraminifera are susceptible to dissolution which may have  
51 limitations. Organic walled dinoflagellate cysts (dinocysts), the resting cysts formed during the sexual reproduction process of  
52 these taxa, are characterized by resistant organic matter and are also generally well preserved in marine sediments (Dale, 1996;  
53 Zonneveld et al., 2013). The well-known correlation of modern dinocyst distribution with distinct physical marine water  
54 properties such as sea surface temperature (SST), salinity, nutrients and productivity indicates the value of dinocysts as a proxy  
55 in paleoceanographic reconstruction, although current research on dinocysts in the South China Sea remains largely confined  
56 to their modern distribution in marine surface sediments (Li et al., 2018a; Li et al., 2020; Li et al., 2023). Fossil dinocyst  
57 records in the SCS are scarce (Li et al., 2021; Li et al., 2017).

58 Given the complementary strengths of different archives, we adopt a multiproxy approach in this study, combining  
59 palynological indicators (pollen, spores, microcharcoal, and dinocysts), organic geochemical proxies (TOC and TN), and  
60 inorganic geochemical markers (element ratios,  $\delta^{13}\text{C}$  and  $\delta^{18}\text{O}$ , and Mg/Ca-based SST of planktonic foraminifera) to  
61 reconstruct vegetation, fire regimes, sediment sources, ocean productivity, and sea surface temperature. A marine sediment  
62 core (SCS-GC-1; Fig. 1a) recovered from the northern SCS was analyzed to reconstruct millennial-scale climate and ocean  
63 dynamics over the last 33 ka. The specific aims of this study are: (1) to reconstruct the palaeovegetation and palaeoclimate; (2)  
64 to document the evolution of palaeoceanographic conditions; and (3) to clarify the mechanisms governing land-ocean  
65 interactions across glacial-interglacial transitions.



66 **Figure 1:** (a) Map of the East Asian monsoon system and ocean circulations with annual modern mean annual sea surface  
67 temperature (Data from World Ocean Atlas, 2023) and the location of core SCS GC-1 (red) retrieved from the northern SCS.  
68 (b) Map of the distribution of vegetation types in the main areas around the South China Sea retrieved from Stibig et al. (2007)  
69 and <https://forobs.jrc.ec.europa.eu/products/glc2000/products.php>. The black solid line indicates the position of the winter  
70 surface current, the white dashed line is the position of the summer surface current, the purple dashed line is the deep current,  
71 and the blue solid line is the Kuroshio Current.



## 73 **2 Environmental setting**

### 74 **2.1 Atmospheric circulation and climate**

75 The northern SCS experiences a subtropical to tropical climate that is primarily governed by the seasonal East Asian Monsoon  
76 system: northeasterly winds prevail during winter (December–February) and southwesterlies dominate in summer (June–  
77 August) (Chao et al., 1995; Wang et al., 2017). In winter, decreasing temperatures over the Asian continent lead to the  
78 development and intensification of a cold high-pressure system over Inner Mongolia, while the Aleutian Low strengthens over  
79 the North Pacific. The resulting continent-ocean pressure gradient drives the East Asian Winter Monsoon (EAWM),  
80 transporting cold, dry northeasterly air masses southwards across China into the SCS. In summer, this pattern reverses: the  
81 continental system is replaced by the Indian Low, and stronger high-pressure systems develop over the North Pacific and the  
82 Australian region, generating the East Asian Summer Monsoon (EASM), which advects warm, moist-laden air from the ocean  
83 onto the Chinese mainland (Liu et al., 2016a).

### 84 **2.2 Oceanic circulation**

85 Surface currents in the SCS are controlled by seasonal variations in the dominant wind directions related to the EASM and  
86 EAWM (Hu et al., 2000), monsoon-topography interactions, and additional influences from wind-stressed eddies. During  
87 winter, the EAWM drives a strong southward western boundary current along the Vietnamese and southern Chinese coasts,  
88 associated with a basin-scale cyclonic circulation. In contrast, summer circulation is weaker and more complex, with coastal  
89 currents generally reversing to flow northward under EASM influence.

90 The EASM drives distinct northern and southern circulation patterns in the SCS, which form two anticyclonic eddies separated  
91 near 12°N by a strong upwelling off Vietnam (Fang et al., 1998). In addition, the region is influenced by the intrusion of warm,  
92 saline Kuroshio waters entering through the Luzon strait between Luzon from Taiwan (Huang et al., 2025).

93 Seasonal variations in marine primary productivity are primarily modulated by the East Asian Monsoon (Liu et al., 2002).  
94 During winter, stronger northeasterlies induce eutrophic conditions in the upper euphotic layer, elevating marine primary  
95 productivity. In summer, persistent heating of warmer, lower-density surface waters intensifies stratification, leading to  
96 oligotrophic conditions and reduced primary productivity (Liu et al., 2002; Zhang et al., 2016).

### 97 **2.3 Vegetation**

98 Vegetation types on the adjacent continental landmass around the SCS are diverse and reflect regional climate conditions (Luo  
99 and Sun, 2013), although they are dominated by tropical and subtropical broadleaved evergreen forests (Fig. 1b) (Stibig et al.,  
100 2007). Whereas tropical rain forest vegetation occurs at low altitudes on tropical islands along the southern coast of the Chinese  
101 mainland, e.g., Hainan Island, and southern Taiwan Island, tropical monsoon forests are distributed widely throughout the  
102 Indochina Peninsula and along the coast of southeastern China. Subtropical evergreen forests are prominent between 24°N and  
103 25°N on southeast-facing hills and on high plateaus (Wang, 1961; Whitmore, 1985). Generally, the abundance of both tropical  
104 and subtropical taxa increase gradually towards the south in eastern China, indicating the significance of the north-south  
105 temperature gradient (Dai and Weng, 2015; Dai et al., 2015). The vegetation types occurring in southeast and southern China,  
106 as well as Taiwan Island, are the main pollen sources of the northern SCS (Dai and Weng, 2011; Sun et al., 1999).

### 107 **2.4 Sedimentation rates**

108 The SCS receives enormous amounts of terrigenous sediments (ca.  $700 \times 10^6$  tons/year) every year, mainly during the rainy  
109 season in summer. The sediments originate from the erosion/weathering of rocks in the catchment basins particularly from  
110 three Asian rivers (the Red River, the Pearl River, and the Mekong River) which are among the largest in the world (Liu et al.,  
111 2010; Milliman and Syvitski, 1992). Beyond the river deltas, part of the terrigenous sediments is deposited on the shelves  
112 (Zhong et al., 2017), while the rest reaches the open sea where the sediment is transported by the oceanic currents and deposited  
113 on the continental slope and in the deep basins (Liu et al., 2013).



### 114 3. Materials and methods

#### 115 3.1 Materials and chronological analysis

116 The 305 cm long marine sediment core SCS GC-1 was retrieved from the northern SCS during R/V Songhang (Shanghai  
117 Ocean University) cruise in October 2022 (18.47°N, 116.34°E; water depth of 3764 m) (Fig. 1).

118 Eight accelerator mass spectrometry AMS  $^{14}\text{C}$  dates at depths of 20 cm, 45 cm, 65 cm, 90 cm, 107 cm, 133 cm, 203 cm and  
119 275 cm were obtained on mixed planktic foraminiferal (including *Globigerinoides ruber*, *Globigerinoides sacculifer*,  
120 *Neogloboquadrina dutertrei*, *Pulleniatina obliquiloculata*, *Orbulina universa*) tests isolated from the core. AMS  $^{14}\text{C}$   
121 measurements were carried out on a NEC 0.5Mev  $^{14}\text{C}$  AMS (National Electrostatics Corporation, NEC) at Guangzhou Institute  
122 of Geochemistry, Chinese Academy of Sciences (GIGCAS).

#### 123 3.2 X-ray fluorescence (XRF) analysis

124 The core was non-destructively scanned using the Avaatech XRF Core Scanner at the State Key Laboratory of Marine Geology,  
125 Tongji University. The parameters of the Avaatech XRF core scanner were set for 30 s exposure time, three voltage and current  
126 conditions with 10 kV and 0.75 mA for Al-Fe, 30 kV and 0.5 mA for Co-Mo, and 50 kV and 0.2 mA for Tc-U. The scanning  
127 area was 5 mm (length)  $\times$  10 mm (width), and at a scanning time of 30 s. The relative content of each element including Al to  
128 Ba which was obtained, is expressed in cps as counts per second.

#### 129 3.3 TOC and TN analysis

130 Approximately 1 g of each freeze-dried sample was treated with diluted 3 mol/L HCl for 24 hours at room temperature to  
131 remove inorganic carbonates. After the reaction, the samples were repeatedly rinsed with ultrapure water (<18 M $\Omega$ ·cm) and  
132 centrifuged until the supernatant reached a neutral pH. The remaining residue was oven-dried at 60°C, ground and then  
133 weighed. The decarbonated samples were analyzed for elemental content using a Vario EL cube elemental analyzer (Elementar,  
134 Germany) at the State Key Laboratory of Marine Geology, Tongji University, employing the dry combustion method.  
135 Replicate analyses were conducted to ensure data reliability, with average standard deviations of  $\leq 0.1$  wt% for both TOC and  
136 TN measurements.

#### 137 3.4 Planktonic foraminiferal isotopic and Mg/Ca analysis

138 The samples were freeze-dried, disaggregated by soaking in water for 1-2 days, then were rinsed repeatedly through a 63  $\mu\text{m}$   
139 sieve to remove organic matter and fine impurities. The rinsed wet samples were then dried at 60°C (approximately 24 h) and  
140 passed through a 125  $\mu\text{m}$  and 250  $\mu\text{m}$  sieve, respectively (Schönfeld et al., 2012). *G. ruber* larger than 250  $\mu\text{m}$  size were  
141 selected under a microscope. For each sample, clean and intact *G. ruber* (around 30 specimens) were picked and tested using  
142 a Finnigan MAT253 Mass Spectrometer. The  $\delta^{18}\text{O}$  results are reported versus VPDB after calibration with NBS 19. The  
143 average test accuracy is  $\pm 0.07\text{‰}$ .

144 For the Mg/Ca analysis, surface dwelling foraminiferal species with smooth-surface individuals of *G. ruber* between 250-350  
145  $\mu\text{m}$  (ca. 0.3 mg) were picked to ensure no obvious contamination or damage, and that the atrioventricular structure was intact  
146 (Barker et al., 2003). The analysis was performed on a quadrupole inductively coupled plasma mass spectrometry (ICP-MS).  
147 Duplicate measurements of two samples yield an average relative deviation of 0.064 mmol/mol, confirming that analytical  
148 uncertainty is minimal and does not materially affect interpretation. Sea surface temperatures were reconstructed following  
149 Eq. (1) (Huang et al., 2008):

$$150 \text{ SST} = 0.5 * (\text{Ln}(\text{Mg/Ca}/0.3)/0.09 + \text{Ln}(\text{Mg/Ca}/(0.38 - 0.02 * D))/0.09) \quad (1)$$

151 Where SST represents mean annual sea surface temperature (°C), Mg/Ca is the *G. ruber* based Mg/Ca ratio (mmol/mol), D is  
152 water depth of the core (km).



153 **3.5 Palynological analysis**

154 In total, 61 samples (mean interval 4 cm) were processed for palynological analysis at Shanghai Ocean University following  
155 standard preparation procedures. Samples were treated sequentially with 10% HCl, 40% HF, 30% HCl, sieved with 125 µm  
156 and 7 µm meshes, and mounted for microscopic examination. Routine identification was performed under a ZEISS Promostar  
157 3 microscope at 400x magnification, with 1000x used for detailed taxonomic identification. Four *Lycopodium* spore tablets  
158 with  $10315 \pm 845$  spores were added to each sample prior to processing to enable calculation of pollen concentration. Pollen  
159 taxa were identified using the reference of Tang et al. (2020). At least 300 pollen grains (including terrestrial pollen taxa,  
160 sedges and aquatic taxa) were counted for most of the samples. The percentages of pollen taxa were calculated based on the  
161 pollen sum, and the percentages of spore taxa were calculated based on pollen and spore sum.

162 Charcoal particles were identified and counted on the same microscope slides prepared for pollen analysis. Only particles  
163 which were black, opaque and angular were considered as charcoal. Particles smaller than 10 µm were not counted due to the  
164 risk of false identification (Mooney and Tinner, 2011). More than 1500 charcoal particles (with an average of 3500 particles)  
165 were counted for each sample. Two size classes were defined, based on the length of the long axis of each fragment: 10-100  
166 µm is assumed to relate to the regional fire signal and >100 µm to local fire signals (Conedera et al., 2009). Charcoal  
167 accumulation rates (particles/cm<sup>2</sup>/yr) were calculated by applying the sediment accumulation rates interpolated from the  
168 radiocarbon age-depth model. The charcoal accumulation rate is a proxy for burned biomass which can represent changes in  
169 the amount of biomass burned or the number of fire occurrences (Aleman et al., 2013).

170 Organic-walled dinoflagellate cysts (dinocysts) were identified based on Zonneveld et al. (2013), DINOFLAJ3 (Williams et  
171 al., 2017), and the online modern dinocyst determination key, viz Zonneveld and Pospelova (2015) and references therein. The  
172 percentage of each taxon was calculated based on the total number of dinocysts. All identified dinocyst taxa and their motility  
173 affinities are listed in Table S1. In addition to the above content, foraminiferal organic linings, and other non-pollen  
174 palynomorphs such as fungal spores were counted. All counts of pollen, microcharcoal and dinocysts as well as other data  
175 discussed in this study have been submitted in the Pangaea database (<https://pangaea.de>) (Felden et al., 2023).

176 **3.6 Statistical analysis**

177 The dinocyst data were analyzed statistically using the CANOCO software (Canonical Community Ordination: version 5) (ter  
178 Braak and Smilauer, 2012). The percentage data used for statistical analysis was not transformed. A Detrended Correspondence  
179 Analysis (DCA) was first conducted to test the distribution of the dataset (unimodal or linear). The longest gradient of DCA  
180 analysis was found to be 1.1 for pollen data and 1.5 for dinocyst data with standard deviations both less than 3, suggesting that  
181 the linear model is more suitable. Accordingly, Principal Component Analysis (PCA) was performed to determine the  
182 relationship between relative abundances of pollen and dinocyst taxa, respectively. Assemblage zones were determined using  
183 the constrained cluster analysis (CONISS) in the TILIA (3.0.1) software (Grimm, 2015), including all counted pollen and  
184 dinocyst taxa with the exception of the top two samples in which insufficient dinocysts were found.

185 **4. Results**

186 **4.1 Age-depth model**

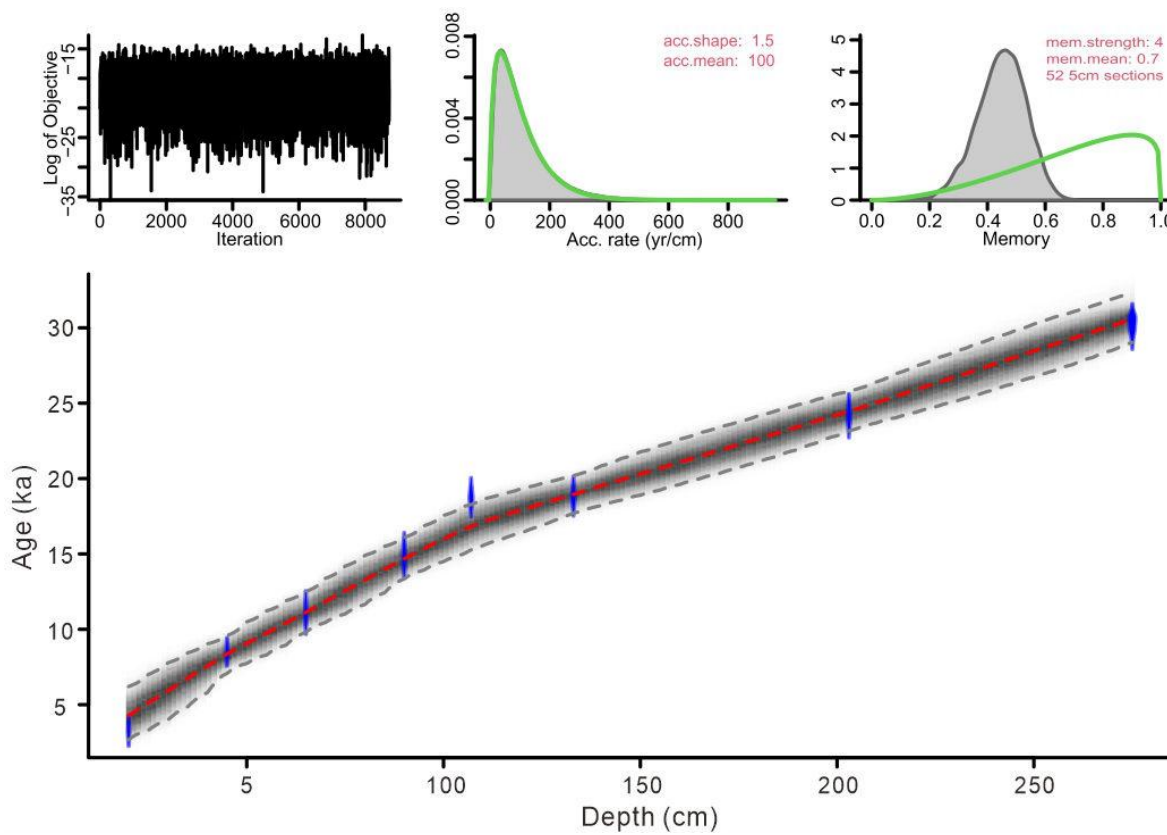
187 The eight <sup>14</sup>C AMS measurements exhibit a systematic increase in radiocarbon age with sediment depth (Table 1). The age-  
188 depth model was constructed using the eight AMS <sup>14</sup>C measurements in a Bayesian framework implemented in Bacon (Blaauw  
189 and Christen, 2011). A prior accumulation rate of 100 yr/cm (shape = 1.5, normal distribution) was applied, with the core  
190 divided into 52 depth sections of 5 cm. The default memory parameter was retained. Posterior weighted mean calibrated ages  
191 were used to derive linear sedimentation rates. The resulting model indicates a basal age of ~33 ka for core SCS GC-1, with  
192 sedimentation rates ranging between 0.005 and 0.013 cm/yr (Figs. 2 and 3a).



194 **Table 1:** AMS  $^{14}\text{C}$  measurement for mixed planktonic foraminifera from the core SCS GC-1.

Lab #	Depth (cm)	Material	$^{14}\text{C}$ age (yr BP)	Calibrated age median (cal. yr BP)	cal. $^{14}\text{C}$ age (cal. yr BP, $\pm 2\sigma$ )
GZ10650	20	mixed species	3420 $\pm$ 25	3036	1810-4285
GZ10651	45	mixed species	8005 $\pm$ 35	8289	7260-9443
GZ10652	65	mixed species	10055 $\pm$ 50	10868	9533-12260
GZ10653	90	mixed species	13090 $\pm$ 70	14708	13392-16057
GZ10654	107	mixed species	15950 $\pm$ 70	18342	17138-19485
GZ10655	133	mixed species	16000 $\pm$ 90	18399	17185-19555
GZ10656	203	mixed species	20540 $\pm$ 170	23656	22496-24875
GZ10657	275	mixed species	26700 $\pm$ 350	29977	28806-31063

195 # yr BP denote before present (1950 AD); all age data were calibrated using the software Calib.Rev.8.10 (Stuiver and Reimer,  
196 1993) and Marine 20 (Hughen et al., 2004). The standard marine reservoir age with a local modification ( $\Delta R = 71 \pm 499$  yr) in  
197 the northern South China Sea was applied (Wan and Jian, 2014).



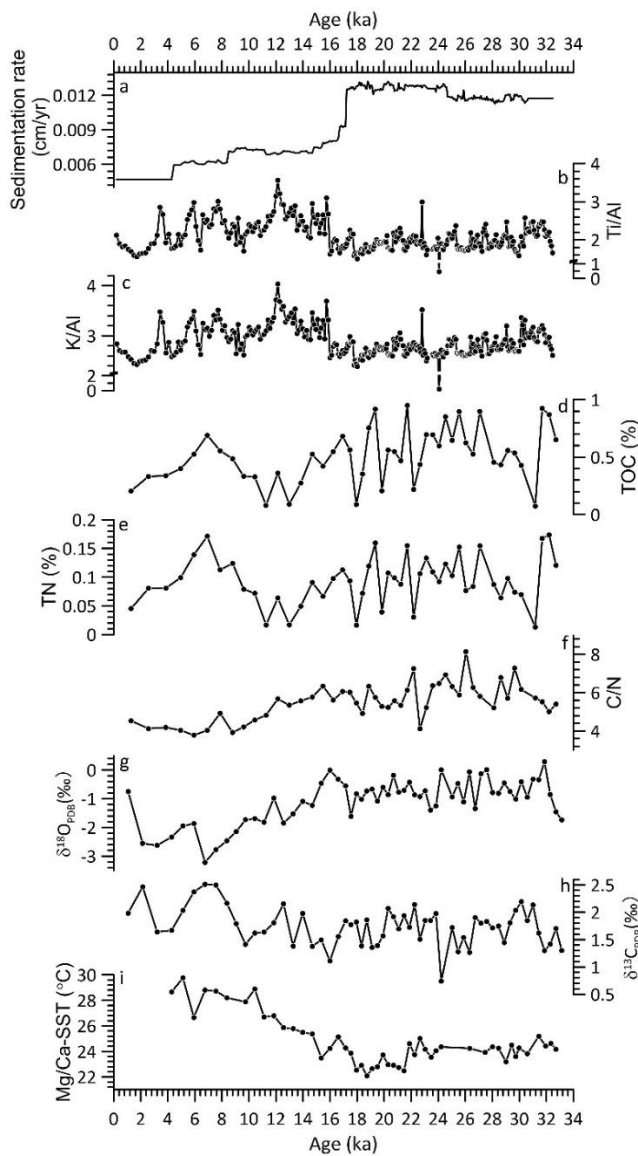
198

199 **Figure 2:** Bayesian age-depth model based on eight AMS  $^{14}\text{C}$  dates from core SCS GC-1: the blue areas represent the 95%  
200 probability distributions of the calibrated ages; the thin red line shows the weighted mean ages, and the blackish-gray area  
201 shows the 95% age-depth relations as modeled by the R software package Bacon 2.2 (Blaauw and Christen, 2011).



202 **4.2 XRF record**

203 The relative contents of these six elements are found for Fe ( $5 \times 10^3$  -  $750 \times 10^3$  cps, mean =  $540 \times 10^3$  cps), Ca ( $0.7 \times 10^3$  -  $650 \times 10^3$  cps, mean =  $190 \times 10^3$  cps), K ( $1.5 \times 10^3$  -  $166 \times 10^3$  cps, mean =  $91 \times 10^3$  cps), Si ( $1 \times 10^3$  -  $144 \times 10^3$  cps, mean =  $71 \times 10^3$  cps) followed by Ti ( $2 \times 10^3$  -  $68 \times 10^3$  cps, mean =  $41 \times 10^3$  cps) and Al ( $0.5 \times 10^3$  -  $14 \times 10^3$  cps, mean =  $6 \times 10^3$  cps) (Fig. S1). Similar patterns among terrigenous elements Fe, K, Ti, Al and Si were observed together with a clearly opposite pattern of marine origin element Ca. The Ti/Al and K/Al show similar patterns with significant correlation ( $r = 0.94$ ,  $P < 0.001$ ) throughout the record (Figs. 3b and 3c), with low values prior to 16 ka and then increase quickly to much higher values after 16 ka with gradually decreasing trend to the end of the record.



210

211 **Figure 3:** Core SCS GC-1 sedimentation rate (a), major element ratio (b-c), contents of total organic carbon (TOC, d) and  
212 nitrogen (TN, e), TOC/TN ratio (f), stable carbon  $\delta^{13}\text{C}_{\text{VPDB}}$  (g) and oxygen  $\delta^{18}\text{O}_{\text{VPDB}}$  (h) isotopes of planktic foraminifera, and  
213 Mg/Ca-SST (i).



## 214 4.3 TOC, TN and C/N record

215 TOC content and the TOC/TN ratio exhibit significant fluctuations throughout the record (Figs. 3d, 3e and 3f). The period  
216 prior to 14.7 ka is characterized by high TOC content with low values around 31.2 ka, 22.2 ka, 19.8 ka, 17.9 ka. After 14.7 ka,  
217 TOC decreased until 10.4 ka when it increased again to a high level around 6.9 ka followed by a decline trend until the top of  
218 the record. Similarly, TOC/TN ratio also exhibits high values prior to 14.7 ka, which then decreased to minimum between 8.8-  
219 5.9 ka interrupted by a brief increase around 7.9 ka.

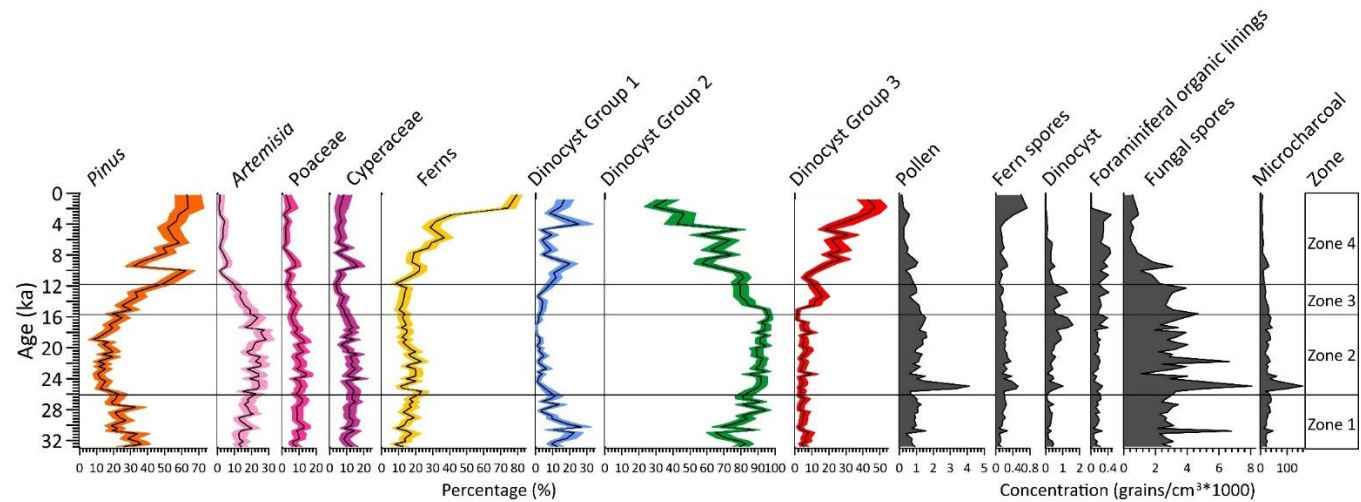
## 220 4.4 Planktonic foraminiferal isotopic and Mg/Ca-SST record

221 The  $\delta^{18}\text{O}$  values of planktonic foraminifera *G. ruber* shells range from  $-3.2\text{\textperthousand}$  to  $0.3\text{\textperthousand}$  (mean =  $-1.1\text{\textperthousand}$ ) with higher values  
222 prior to 16 ka, then rapidly decreasing to much lower values (Fig. 3g). The  $\delta^{13}\text{C}$  values range from  $0.7\text{\textperthousand}$  to  $2.5\text{\textperthousand}$  (mean =  $1.7\text{\textperthousand}$ )  
223 with relatively low values prior to 16 ka (Fig. 3h), there after increasing but with substantial variation.

224 Mean Mg/Ca-derived SSTs range from  $22.1^\circ\text{C}$  to  $29.7^\circ\text{C}$  (mean =  $24.8^\circ\text{C}$ ) across the core (Fig. 3i). Relatively low values  
225 ( $23.2\text{--}25.2^\circ\text{C}$ , mean =  $24.2^\circ\text{C}$ ) occur prior to 21.9 ka, followed by a further decline to the lowest values ( $22.1\text{--}24.6^\circ\text{C}$ , mean =  
226  $23.1^\circ\text{C}$ ) between 21.9-17.5 ka. After  $\sim 15.4$  ka, SSTs increase progressively toward the highest values observed in the record  
227 ( $23.5\text{--}29.7^\circ\text{C}$ , mean =  $26.8^\circ\text{C}$ ).

## 228 4.5 Palynological record

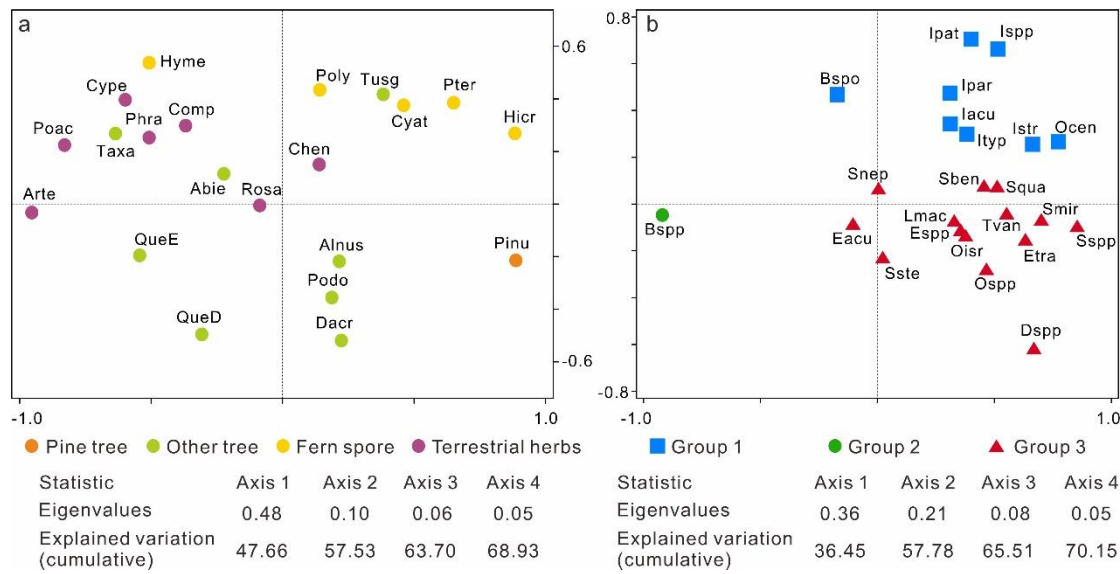
229 The complete diagram of pollen, charcoal and dinocyst results are shown in Figs. S2 and S3. Pollen preservation is variable,  
230 with particularly high concentrations ( $390\text{--}4100$  grains/ $\text{cm}^3$ ; mean =  $1200$  grains/ $\text{cm}^3$ ) prior to 16.1 ka, and highest  
231 concentrations around 25.3-25.0 ka ( $3300\text{--}4100$  grains/ $\text{cm}^3$ ; mean =  $3700$  grains/ $\text{cm}^3$ ) (Fig. 4). Similarly, charcoal exhibits the  
232 highest concentrations ( $36\text{--}155 \times 10^3$  particles/ $\text{cm}^3$ ; mean =  $83 \times 10^3$  particles/ $\text{cm}^3$ ) around 25.3-23.7 ka, decreasing after 15.6  
233 ka, reaching minimum values at the top of the core ( $9\text{--}31 \times 10^3$  particles/ $\text{cm}^3$ ; mean =  $21 \times 10^3$  particles/ $\text{cm}^3$ ) (Fig. 4). Dinocyst  
234 concentrations are relatively low, ranging from  $7\text{--}1600$  cysts/ $\text{cm}^3$  (average of  $450$  cysts/ $\text{cm}^3$ ) with high values of  $110\text{--}1600$   
235 cysts/ $\text{cm}^3$  (average of  $650$  cysts/ $\text{cm}^3$ ) between 25.6-11.7 ka (Fig. 4). After 11.7 ka, dinocyst concentrations decrease, reaching  
236 a minimum at the end of the record.



237  
238 **Figure 4:** Percentages of dominated pollen taxa, including tree pollen *Pinus*, terrestrial pollen *Artemisia*, Poaceae and  
239 Cyperaceae, fern spores, and three dinocyst groups based on principal component analysis (PCA) analysis, concentrations  
240 (grains/ $\text{cm}^3 \times 1000$ ) of pollen, fern spores, dinocyst, foraminiferal organic linings, fungal spores and microcharcoal  
241 concentration (particles/ $\text{cm}^3 \times 1000$ ).



242 According to the PCA results (Fig. 5a), pollen and spore taxa are well-separated based on their associated biomes. Specifically,  
 243 *Pinus* and fern spore (notably *Hicriopteris*) form a distinct cluster on the positive end of axis 1, while characteristic terrestrial  
 244 herbs (particularly *Artemisia*, Poaceae and Cyperaceae) are separated along the negative end of axis 2. Three groups of dinocyst  
 245 taxa can be distinguished based on the PCA results, showing clearly different trends across the record (Fig. 5b). Group 1:  
 246 *Operculodinium. centrocarpum*, *Impagidinium* spp., *Impagidinium aculeatum*, *Impagidinium patulum*, *Impagidinium*  
 247 *paradoxum*, *Impagidinium strialatum*, *Impagidinium* type1; *Bitectatodinium spongium*; Group 2: *Brigantedinium* spp.; Group  
 248 3: *Echinidinium* spp., *Echinidinium aculeatum*, *Echinidinium transparantum*, *Selenopemphix nephroides*, *Stellasinium*  
 249 *stellatum*; *Selenopemphix quanta*, *Dubridinium* spp., *Operculodinium israelianum*; *Operculodinium* spp., *Lingulodinium*  
 250 *machaerophorum*, *Tuberculodinium vancampoae*, *Spiniferites mirabilis*, *Spiniferites* spp.; *Spiniferites bentori*.



251 **Figure 5:** Results of the principal component analysis (PCA) illustrating the ordination of pollen (a) and dinocyst taxa (b) from  
 252 core SCS GC-1 with colored symbols referring to the groups. For pollen, pine tree (orange): Pinu (*Pinus*); other tree (light  
 253 green): QueE (*Quercus* evergreen), QueD (*Quercus* deciduous), Alnu (*Alnus*), Podo (*Podocarpaceae*), Dacr (*Dacrycapus*),  
 254 Taxa (*Taxaceae*), Abie (*Abies*), Tusg (*Tusga*); fern spores (yellow): Hicr (*Hicriopteris*), Pter (*Pteris*), Cyat (*Cyatheaceae*),  
 255 Poly (*Polypodiaceae*), Hyme (*Hymenophyllaceae*); terrestrial herbs (purple): Arte (*Artemisia*), Poac (*Poaceae*), Cype  
 256 (*Cyperaceae*), Comp (*Compositae*), Phra (*Phragmites*), Chen (*Chenopodiaceae*), Rosa (*Rosaceae*). For dinocyst groups,  
 257 Group 1 (blue): Ocen (*O. centrocarpum*), Ispp (*Impagidinium* spp.), Iacu (*Impagidinium aculeatum*), Ipat (*Impagidinium*  
 258 *patulum*), Ipar (*Impagidinium paradoxum*), Istr (*Impagidinium strialatum*), Ityp (*Impagidinium* type1); Bspo (*Bitectatodinium*  
 259 *spongium*); Group 2: Bspp (*Brigantedinium* spp.); Group 3: Espp (*Echinidinium* spp.), Eacu (*Echinidinium aculeatum*), Etra  
 260 (*Echinidinium transparantum*), Snep (*Selenopemphix nephroides*), Sste (*Stellasinium stellatum*); Squa (*Selenopemphix*  
 261 *quanta*), Dspp (*Dubridinium* spp.), Oisr (*Operculodinium israelianum*); Ospp (*Operculodinium* spp.), Lmac (*Lingulodinium*  
 262 *machaerophorum*), Tvan (*Tuberculodinium vancampoae*), Sben (*Spiniferites bentori*); Smir (*Spiniferites mirabilis*); Sspp  
 263 (*Spiniferites* spp.).

265 Based on the variations in percentage and concentration values of pollen, dinocyst and charcoal as well as the CONISS analysis,  
 266 four zones can be recognized (Fig. S2):

#### 267 4.5.1 Zone SCS GC-1 1 (301-217cm, 32.8-25.6 ka)

268 This zone is characterized by relatively high percentages of *Pinus* and *Quercus* (evergreen), while pollen taxa of terrestrial  
 269 herbs such as *Artemisia*, Poaceae and Cyperaceae as well as fern spores including *Hicriopteris*, *Polypodiaceae*, *Cyatheaceae*  
 270 are relatively low (Fig. 4 and Fig. S2). High fungal spore concentrations here coincide with low charcoal concentrations. The



271 percentages of heterotrophic taxa *Brigantedinium* spp. (Group 1) increase gradually to the end of this zone, whereas the  
272 percentages of autotrophic taxa (Group 2) particularly *Impagidinium* species reach their maximum levels in the record but  
273 decline towards the end of this zone (Fig. 4 and Fig. S2). Concentrations of foraminiferal organic linings reach minimum in  
274 this zone.

275 **4.5.2 Zone SCS GC-1 2 (217-97 cm, 25.6-15.6 ka)**

276 The percentage of *Pinus* pollen decreases to its lowest values of the entire record. Meanwhile, terrestrial herb taxa, particularly  
277 *Artemisia*, increase to their highest levels along with fungal spores. Some fern spore types, including *Polypodiaceae*,  
278 *Hymenophyllaceae*, *Cyatheaceae* and *Pteris*, also exhibit relatively high values compared to Zone SCS GC-1 1 (Fig. 4 and Fig.  
279 S2). Concentrations of pollen, fern spores and charcoal all reach maximum values, peaking around 25.3-24.3 ka when dinocyst  
280 concentrations also exhibit a maximum, along with *Brigantedinium* spp. On the other hand, Group 1 dinocyst taxa are at  
281 minimum values in this zone. Concentrations of foraminiferal organic linings remain at low value in this zone.

282 **4.5.3 Zone SCS GC-1 3 (97-69 cm, 15.6-11.7 ka)**

283 This zone is characterized by the rapid increase in *Pinus* pollen, accompanied by a sharp decline in terrestrial herbs, especially  
284 *Artemisia*. Concentrations of fungal spores exhibit a declining trend and return to the levels observed in Zone SCS GC-1 1.  
285 Concentrations of pollen, fern spores and charcoal also exhibit a declining trend to reach near the lowest levels, whereas  
286 dinocyst concentrations remain relatively prominent. However, the percentage of *Brigantedinium* spp. exhibits a decline in  
287 this zone, accompanied by a marked increase of Group 3 taxa, including *Dubridinium* spp. and *Echinidinium* spp. Meanwhile,  
288 dinocysts in Group 2 achieve relatively high values. Concentrations of foraminiferal organic linings increase gradually from  
289 the beginning of this zone.

290 **4.5.4 Zone SCS GC-1 4 (69-0 cm, 11.7 ka-present)**

291 The percentages of *Pinus* pollen reach their highest values of the entire record interrupted around 9.5-9.0 ka by a very marked  
292 decline to values close to those of Zone SCS GC-1 1. The abrupt reduction in *Pinus* pollen is also observed in the overall  
293 pollen, fungal spore, charcoal concentration, and in terrestrial herb pollen especially. Additionally, this zone is characterized  
294 by the increase in fern spores, particularly *Hicriopteris* which exhibits a short, sharp increase around 2.8 ka (Fig. 4 and Fig.  
295 S2). The percentage of *Brigantedinium* spp. decreases to the lowest values of the entire record, whereas the percentage of  
296 Group 3 dinocyst taxa, along with the concentration of foraminiferal organic linings all reach their highest values.

297 **5. Discussion**

298 **5.1 Environmental significance of key proxies**

299 **5.1.1 K/Al and Ti/Al**

300 In comparison to single elements, elemental ratios which are insensitive to dilution effects, are more useful as environmental  
301 indicators (Govin et al., 2012). Ti is highly enriched in mafic and volcanic rocks, while Al is a major component of most  
302 common clay mineral found in all types of weathered continental crust. The SCS is surrounded by diverse geological terrains  
303 with distinct Ti/Al ratios originating from different sources such as the Luzon Volcanic Arc (Philippines), Taiwan and other  
304 basaltic sources with high Ti/Al, while with low Ti/Al originating from the major continental river systems that drain ancient,  
305 weathered landmasses. Thus, Ti/Al can provide a robust picture of terrestrial input and its origin in the complex environment  
306 of the SCS. High Ti/Al indicates increased relative input of sediment from a volcanic or mafic source/less chemical, and low  
307 Ti/Al indicates increased relative input of sediment from a felsic continental source (e.g., Pearl River, Mekong River) (Hu et  
308 al., 2013; Wan et al., 2007). K/Al and Ti/Al records of ODP Site 1143 from the SCS generally show low values during glacial



309 periods and high values during interglacial periods, clearly indicating that increase in K/Al and Ti/Al is probably related to  
310 wetter conditions and thus the intensified chemical weathering (Clift et al., 2008; Tian et al., 2011; Wei et al., 2004).

### 311 5.1.2 Source area and transport of pollen and spores

312 In the northern SCS sediments, the modern distribution of tree pollen, particularly *Pinus*, shows disproportionately high  
313 representation relative to other pollen types. This suggests substantial contributions from south and southeast China,  
314 transported primarily by the northeasterly winter monsoon and associated wind-driven currents. While elevated *Pinus*  
315 percentages can signal either a strengthened winter monsoon or a cool, humid climate (Luo et al., 2018; Sun et al., 2003), PCA  
316 results (Fig. 5a) indicate that this ambiguity can be resolved by incorporating fern spore data. Unlike the wind-dispersed *Pinus*  
317 pollen, fern spores are larger, heavier, and primarily transported by river runoff. Their high abundance in sediments therefore  
318 signals a proximal source from humid montane forests (e.g., in Taiwan and Southern China), reflecting a humid climate  
319 controlled by the EASM (Kaars et al., 2000; Sun et al., 2000b; Wang et al., 2009). Consequently, a simultaneous peak in both  
320 *Pinus* pollen and fern spores is incompatible with a scenario of solely strengthened, dry winter winds. Instead, this combined  
321 signal robustly indicates a cool and humid climate, where a vigorous EASM delivered high rainfall (promoting fern-rich  
322 vegetation and riverine spore transport) while the winter monsoon remained active enough to distribute *Pinus* pollen without  
323 dominating the climatic regime. *Artemisia*, Poaceae and Cyperaceae pollen are the main components of terrestrial herbs  
324 observed in the core. *Artemisia* spp. is currently widely distributed in temperate grassland and steppe which is associated with  
325 cool, semi-arid conditions (Bandara et al., 2023; Sun et al., 2003). Although Poaceae and Cyperaceae pollen indicate a range  
326 of different habitats, high percentages of Poaceae pollen in the sediment are suggestive of grassland vegetation, and a high  
327 representation of Cyperaceae pollen typically points to a wetland environment (Sun et al., 2003; Wang et al., 2009).

328 Previous studies have found clear temporal variations in pollen assemblages in the SCS characterized by marked higher pollen  
329 concentrations in glacial sediments than in interglacial sediments (Jiwarungrueangkul and Liu, 2021; Sun et al., 2000a; Sun  
330 and Luo, 2001; Sun et al., 2003; Zheng and Lei, 1999). On one hand, the large amount of pollen in glacial sediments at the site  
331 might be transported by a strengthened northeast winter monsoon from the Asian mainland and Taiwan Island. In contrast,  
332 during the last glacial low stand, sea level was 120–150 m lower than today, exposing much of the northern SCS continental  
333 shelf and increasing land area by roughly 24×104 km<sup>2</sup> (Chen et al., 2020; Sun et al., 2000a; Wang et al., 2009). The northern  
334 SCS would likely receive substantial pollen and spore amounts via wind or water from the exposed continental shelf which  
335 was covered by grassland under the prevailing dry and temperate climate of the time (Luo and Sun, 2005; Sun et al., 2003).  
336 Typically, during glacial periods, herbaceous vegetation is predominant in the region, whereas during interglacial periods tree  
337 and ferns dominate the terrestrial land mass adjacent to the SCS (Sun et al., 2000a; Sun and Luo, 2001). Such glacial-  
338 interglacial transitions are driven by changes in climate, or ocean currents, or both. During MIS 2 (21–11.5 ka), *Artemisia*  
339 increased again and occupied most of the extensive emerged continental shelf (Sun et al., 2003). Accordingly, the ratio of  
340 trees/herb pollen is a valuable indicator of glacial-interglacial cycles along with their associated vegetation and climate  
341 conditions.

### 342 5.1.3 Dinocysts

343 Although modern dinocyst distributions are strongly correlated with sea surface conditions such as sea surface temperature,  
344 sea surface salinity, nutrient levels and productivity (Dale, 1996; Marret and Zonneveld, 2003; Zonneveld et al., 2024),  
345 dinocyst deposition and preservation in marine sediments are affected by various non-ecological, taphonomic factors which  
346 may alter the primary dinocyst accumulation in the sediment (Holzwarth et al., 2007). It is therefore crucial to account for  
347 these factors before relating the fossil dinocyst record to palaeoenvironmental conditions. Upwelling off west Luzon is driven  
348 by the EAWM and intensifies during stronger EAWM phases. This process brings nutrient-rich subsurface waters to the surface,  
349 promoting enhanced dinoflagellate production (Yuan et al., 2004b). The Kuroshio Current, which transports warm and high-  
350 salinity water into the northern SCS leading to a significant increase in sea surface temperature, is also a significant factor  
351 influencing dinoflagellate growth. Additionally, heterotrophic taxa, such as degradation-sensitive species from the  
352 *Protoperidinium* genus, are more susceptible to aerobic degradation compared to autotrophic taxa (Holzwarth et al., 2007).  
353 This may be influenced by the water oxygen content which may therefore alter dinocyst assemblages before and after  
354 sedimentation (Zonneveld et al., 2008). However, the persistent dominance of heterotrophic dinocysts in the record (up to 99%



355 with mean values of 85%) suggests that selective dissolution of protoperidiniacean species relative to other taxa in the  
356 sediments is negligible (Zhao et al., 2017).

357 *Impagidinium* cysts as well as *O. centrocarpum* typically indicate open ocean, fully marine settings characterized by low  
358 primary productivity, low nutrient levels, and well-oxygenated bottom waters (Zonneveld et al., 2013; Zonneveld and  
359 Pospelova, 2015). Modern surface dinocyst distribution in SCS shows that most of *Impagidinium* species, *Nematosphaeropsis*  
360 *labyrinthus* and *Polysphaeridium zoharyi* are positively correlated with water depth. Their highest abundances were observed  
361 in the northern slope-deep basin which is influenced by the Kuroshio Current, indicating an open-ocean environment (Li et al.,  
362 2020). In the northern Philippine Sea, the predominance of *Impagidinium* taxa from the bottom sediments is also indicative of  
363 pelagic and tropical regions (Matsuoka, 1981). During winter, the Kuroshio Current transports high-salinity, low-nutrient  
364 waters from the Philippine Sea through the Luzon Strait, which then flows along the continental shelf break, reaching the study  
365 area in the northern SCS. This provides further evidence that the increased abundance of Group 1 taxa may reflect typical  
366 nutrient-poor open ocean environments. Dinocysts preserved in SCS GC-1 are dominated by *Brigantedinium* spp. (28-96%,  
367 mean = 80%), which have also been observed from sediment trap samples in the southwest Taiwan waters of the SCS with  
368 high representation ranging from 68% to 91% (Li et al., 2018b). High abundances of *Brigantedinium* spp. are characteristic of  
369 increased nutrient supply (Dale, 1996), which has been used as an indicator of primary productivity (Li et al., 2020; Zonneveld  
370 et al., 2013). In addition, *Brigantedinium* spp. is usually more abundant near the winter upwelling zone in the South China Sea  
371 (Li et al., 2020). Therefore, Group 2 taxa, characterized by the dominance of *Brigantedinium* spp., indicates intensified  
372 upwelling conditions with strong terrigenous influence that contrasts with open-ocean oligotrophic conditions indicated by  
373 Group 1. The stratigraphic variation of Group 2 cysts (Fig. 6h) displays an inverse relationship with Mg/Ca-SST, supporting  
374 the glacial 'high-productivity/low-temperature' paradigm. Group 3 taxa, characterized by dinocysts such as *Echinidinium* spp.  
375 and *S. quanta* are typically adapted to fully marine, eutrophic, and highly productive regimes, and are likely indicative of water  
376 column stratification and upwelling processes in open ocean environments (Zonneveld et al., 2013).

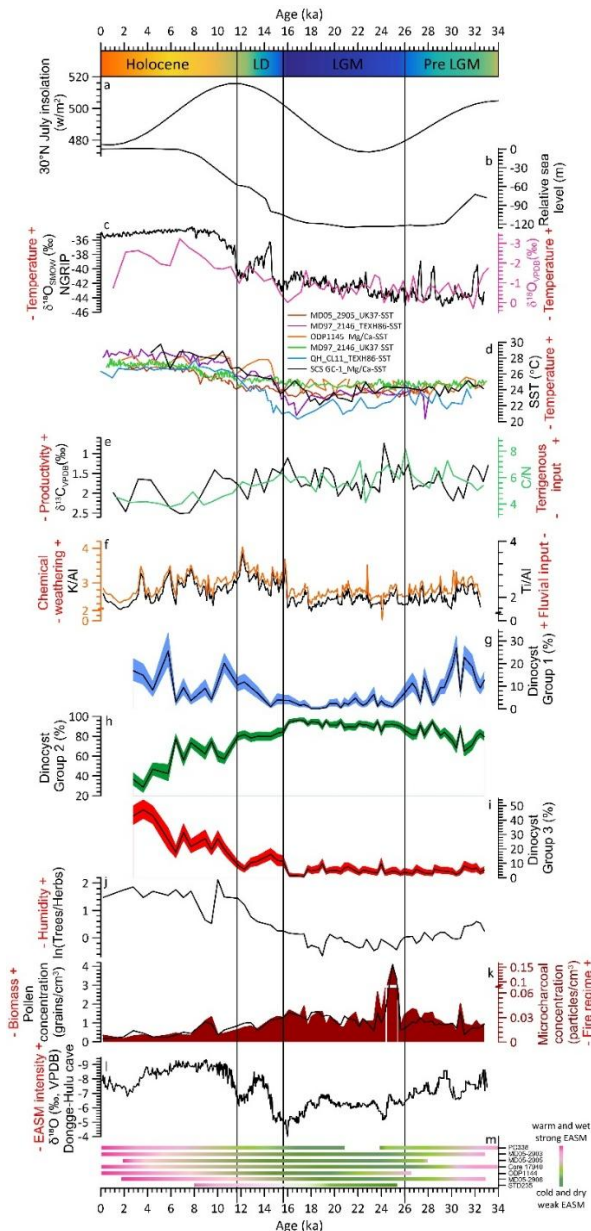
## 377 5.2 Sea level forcing during the LGM

378 Over the past 33 ka, four different periods have been clearly recognized based on our multiproxy record (Fig. 6): pre-LGM  
379 (32.8-25.6 ka), LGM (25.6-15.6 ka), last deglaciation (15.6-11.7 ka) and the Holocene (11.7-present) indicating a distinctive  
380 pattern of glacial-interglacial transition. The pre-LGM phase was characterized by higher sedimentation rates (Fig. 3a), cooler  
381 SST (Figs. 6c and 6d), higher primary productivity (Figs. 6e and 6h), reduced humidity (Figs. 6f, 6j, 6l and 6m), a  
382 predominance of terrestrial herbs (Fig. 6j), and strengthened fire activity (Fig. 6k) which became more pronounced during the  
383 LGM.

384 Previous studies have suggested that elevated charcoal and terrestrial pollen concentrations during the LGM reflect reduced  
385 distance to the sediment source associated with the exposure of the northern SCS continental shelf during glacial low stands  
386 (Luo and Sun, 2005; Sun et al., 2000a). Our data supports this interpretation: the minimum tree/herb ratio (Fig. 6j) indicates  
387 extensive expansion of herbaceous vegetation at the expense of *Pinus* on the exposed shelf surface, which would have supplied  
388 abundant fuel, consistent with the high pollen concentrations (Fig. 6k) and the increased abundance of large charcoal particles  
389 (>100  $\mu\text{m}$ ) (Fig. S3) representing predominantly local fires. Enhanced terrigenous nutrient delivery also appears to have  
390 stimulated marine productivity during the LGM. Elevated  $\delta^{13}\text{C}$  values of planktonic foraminifera (Fig. 6e), increased dinocyst  
391 Group 2 and reduced Group 1 (Figs. 6g-h), together with rising TOC/TN (Fig. 6e), all point to strengthened terrestrial nutrient  
392 supply. A global compilation further shows that OC accumulation rates during glacial maxima were ~50% higher than  
393 interglacial intervals (Cartapanis et al., 2016). The substantially shortened distance between the exposed shelf and the core site  
394 (Lambeck et al., 2014) would have facilitated more efficient transfer of terrigenous nutrients to proximal deep-sea areas. The  
395 low Ti/Al ratios (Fig. 6f) suggest that this enhanced input originated mainly from felsic continental rivers (e.g., the Pearl River).  
396 Although the reduced K/Al (Fig. 6f) and Donge-Hulu cave  $\delta^{18}\text{O}$  records (Fig. 6l) (Wang et al., 2001; Yuan et al., 2004a)  
397 indicate a weakened EASM that would typically suppress fluvial discharge, this appears to have been offset by the markedly  
398 closer coastline and the likely persistence of eolian dust transport from the Chinese mainland. The combined effect of these  
399 terrestrial nutrient sources would have favoured heterotrophic dinoflagellate production (Smayda and Trainer, 2010),  
400 contributing to the observed rise in marine productivity. Independent evidence from the northern SCS similarly links higher



401 glacial productivity to intensified winter winds, enhanced water-column mixing, and upwelling, as well as increased land-  
402 derived nutrient supply (Li et al., 2008).



403

404 **Figure 6:** 30°N July insolation (Laskar et al., 2004) (a); relative sea level on the Sunda Shelf, South China Sea (Hanebuth et  
405 al., 2000) (b); NGRIP  $\delta^{18}\text{O}_{\text{SMOW}}$  (Andersen et al., 2004) (c, black) and stable oxygen  $\delta^{18}\text{O}_{\text{VPDB}}$  of planktonic foraminifera from  
406 SCS GC-1 (c, pink); SST records from MD052905 (Zhou et al., 2012), MD972146 (Lin et al., 2014), ODP1145 (Oppo and  
407 Sun, 2005), QHCL11 (Liu et al., 2020) and SCS GC-1 (d); stable carbon  $\delta^{13}\text{C}_{\text{VPDB}}$  of planktonic foraminifera (e, black) and  
408 C/N ratio (e, green); major element ratio Ti/Al (f, black) and K/Al (f, orange), percentages of three dinocyst groups (g, h, i);  
409 ratio of trees/herbs (j); pollen concentration (k, black) and microcharcoal concentration (k, dark red shading); Dongge-Hulu  
410 cave  $\delta^{18}\text{O}_{\text{PDB}}$  (l) (Wang et al., 2001; Yuan et al., 2004a); summary of records indicating climate and potential intensity of



411 EASM (m) (Sun et al., 2000a; Sun et al., 2000b; Luo and Sun, 2005; Zhou et al., 2012; Xie et al., 2014; Dai and Weng, 2015;  
412 Dai et al., 2015a; Yu et al., 2017; Li et al., 2019). Pre LGM: pre Last Glacial Maximum; LGM: Last Glacial Maximum; LD:  
413 last deglaciation.

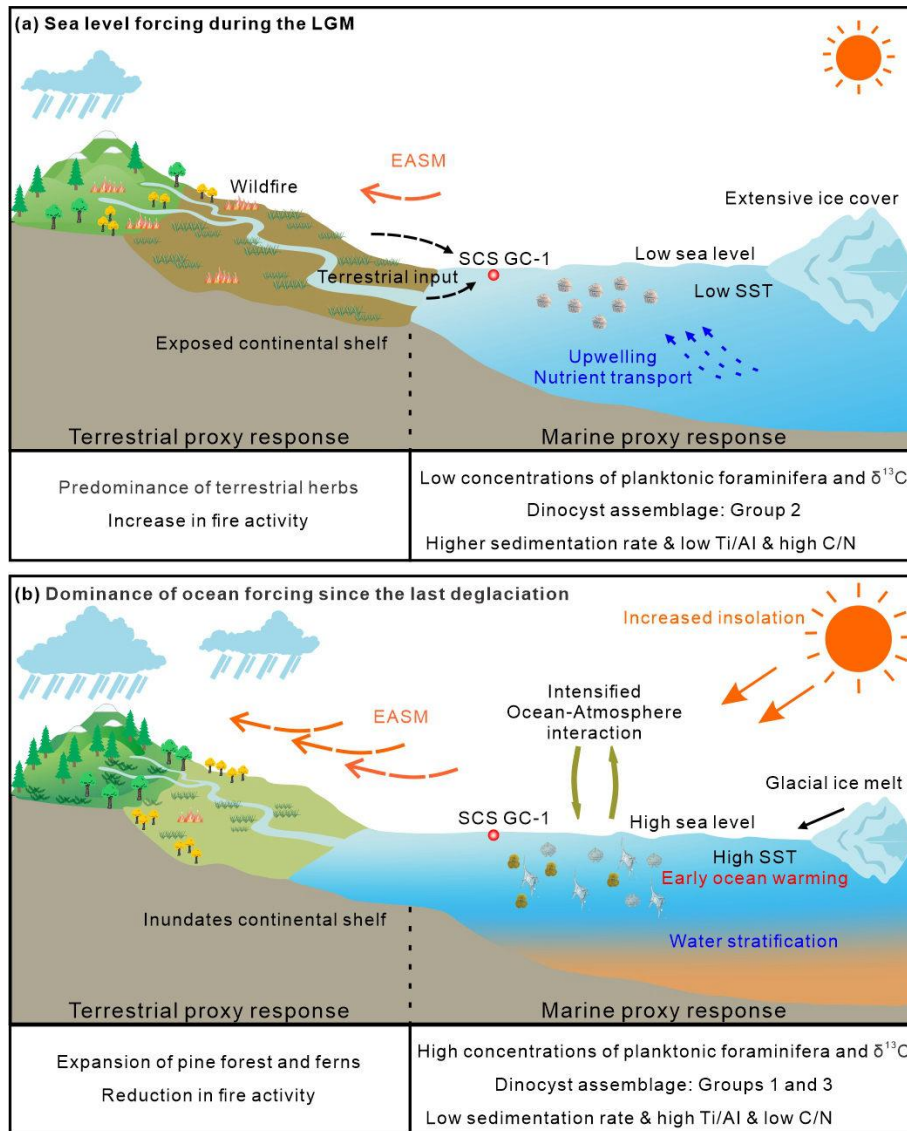
#### 414 **5.3 Dominance of ocean forcing since the last deglaciation**

415 Since the last deglaciation, the northern SCS has experienced a comprehensive environmental transformation characterized by  
416 decreasing sedimentation rates, rising SST, declining primary productivity, increased moisture availability, a pronounced  
417 expansion of pine forests, and minimal fire activity. A key observation is that SST warming in the northern SCS begins ~1.9  
418 ka earlier than changes recorded by the other proxies (Figs. 6c and 6d) (Andersen et al., 2004; Lin et al., 2014; Liu et al., 2020;  
419 Oppo and Sun, 2005; Zhou et al., 2012). This earlier onset corresponds more closely with rising insolation (Fig. 6a) (Laskar  
420 et al., 2004) than with sea-level rise (Fig. 6b) (Hanebuth et al., 2000). This implies that, in addition to the well-recognized role  
421 of sea-level rise, ocean warming likely acted as an initial trigger for subsequent environmental changes. This effect is especially  
422 pronounced in the tropics and is consistent with the concept of tropical ocean-atmosphere forcing (Cheng et al., 2019; Xie et  
423 al., 2010).

424 The mechanisms underlying these changes can be traced through both marine and terrestrial proxies. The rising sea level  
425 reduced the extent of the exposed continental shelf, increasing the distance from terrestrial sediment sources to the core site  
426 (Luo and Sun, 2005; Sun et al., 2000a). Inundation of the continental shelf created a massive sediment trap in newly formed  
427 shallow marine environments, leading to a dramatic reduction in terrigenous material reaching the deep basin (Liu et al., 2003;  
428 Wang and Sun, 1994). This is reflected in markedly lower sedimentation rates and increased Ti/Al ratios (Figs. 3a and 6f),  
429 indicating reduced terrestrial input. At the same time, shrinkage of the continental shelf area constrains the growth of terrestrial  
430 herbs, which were progressively replaced by expanding pine forests and ferns (Figs. 5 and 6j). Relatively high concentrations  
431 of foraminiferal organic linings (Fig. 4) also imply that the water depth and the open ocean environments had become suitable  
432 for planktonic foraminifera (Tyszka et al., 2021). The synchronous strengthening of the EASM, likely initiated by intensified  
433 ocean-atmosphere interactions, is reflected by the rapid negative shift in the Dongge-Hulu Cave  $\delta^{18}\text{O}$  record (Fig. 6l) (Wang  
434 et al., 2001; Yuan et al., 2004a), and is further supported by other paleorecords from the northern SCS (Fig. 6m) (Dai and  
435 Weng, 2015; Dai et al., 2015; Li et al., 2019; Luo et al., 2015; Sun et al., 2000a; Sun et al., 2000b; Xie et al., 2014; Yu et al.,  
436 2017; Zhou et al., 2012). This further supported the vegetation shift by enhancing regional humidity. The wetter conditions  
437 led to a sharp reduction in fire activity, as evidenced by decreased charcoal concentrations (Fig. 6k), while the decline in  
438 coprophilous fungal spores (Lee et al., 2022) suggests a corresponding response in herbivore populations to the changing  
439 landscape (Fig. 4). Similar conditions with increase in fern spores, decrease in terrestrial herbs and dinocyst concentration  
440 were also recorded from 12.5-6.8 ka in the core GLW31D (Li et al., 2017).

441 Likewise, reduced terrestrial input cannot fully explain the marine environmental changes particularly the decreased primary  
442 productivity and shift in dinocyst associations. The early onset of SST warming may have strengthened upper water column  
443 stratification, thereby reduced vertical nutrient supply and contributed to the decline in primary productivity. This  
444 interpretation is supported by the shift in dinocyst assemblages: Group 2 taxa decreases while Group 3 increases, consistent  
445 with more strongly stratified conditions and reduced upwelling relative to the LGM. Periodic peaks in Group 1, particularly  
446 around 10.6 ka and 5.8 ka, further point to an enhanced influence of the warm, nutrient-poor Kuroshio Current (Liu et al.,  
447 2016b), which would additionally suppress productivity. Independent evidence for strengthened Kuroshio intrusion during the  
448 early Holocene is also recorded in core GLW31D from the northern SCS (Li et al., 2021).

449 Collectively, the multi-proxy dataset shows that deglacial environmental transitions in the northern SCS reflect the combined  
450 action and interaction of several forcings rather than a single dominant driver (Fig. 7). Tropical ocean warming initiated the  
451 deglacial transition through both direct marine influence and remote atmospheric feedback, triggering a marked shift in  
452 dinocyst associations and decreased primary productivity through enhanced water column stratification. This was followed by  
453 sea-level rise that reconfigured coastal geography and sediment transport, further reducing terrestrial nutrient input. The  
454 superimposed intensification of the EASM then completed the regional shift to humid conditions, driving vegetation succession  
455 and suppressing fire activity. This multi-mechanism framework highlights the complex yet coherent response of both marine  
456 and terrestrial systems to global climatic changes during the last deglaciation.



457

458 **Figure 7:** A conceptual framework of driving mechanisms and associated environmental responses during the LGM (a) and  
459 since the last deglaciation (b) based on multiproxy record from the core SCS GC-1 in the northern SCS.

## 460 6 Conclusions

461 Our multi-proxy reconstruction from the northern SCS provides a high-resolution record of clear glacial-interglacial climatic  
462 and oceanic transitions over the past 33 ka. Four distinct climatic phases are identified, viz. the pre-Last Glacial Maximum  
463 (32.8-25.6 ka), Last Glacial Maximum (25.6-15.6 ka), last deglaciation (15.6-11.7 ka) and the Holocene (11.7 ka-present). The  
464 glacial intervals (pre-LGM and LGM) were characterized by higher sedimentation rates, cooler SST, higher primary  
465 productivity, herb-dominated landscapes, reduced humidity and intensified fire activity. A fundamental regime shift occurred  
466 during the last deglaciation, marked by evidently decreasing sedimentation rates, rising SST, declining primary productivity,  
467 a pronounced expansion of pine forests, increased moisture availability, and diminished fire activity. The Holocene was



468 characterized by a period of relative stability, defined by the lowest sedimentation rates, warmest SST, highest humidity,  
469 maximum pine forest coverage and minimal fire disturbance. In summary, the combined evidence reveals that the deglacial  
470 environmental changes of the northern SCS were driven by the interplay of multiple forcings including increased insolation,  
471 sea-level rise and monsoon intensification, with ocean warming preceding other changes, suggesting the important role of  
472 tropical ocean-atmosphere interactions in initiating this transition. This study highlights the value of integrated land-sea proxies  
473 in deciphering complex climate interactions and underscores the northern SCS's sensitivity to both high- and low-latitude  
474 forcing. Future research employing a spatial network of cores across the SCS will be crucial to better resolve the spatial patterns  
475 and teleconnections of these changes.

#### 476 **Author Contributions**

477 Xueqin Zhao: Conceptualization, Data curation, Formal analysis, Funding acquisition, Investigation, Methodology, Project  
478 administration, Supervision, Validation, Writing – original draft, Writing – review and editing; Shengjie Ye: Investigation,  
479 Visualization, Writing – review and editing; Jiahui Yao: Investigation, Formal analysis, Writing – review and editing; Michael  
480 Meadows: Validation, Writing – review and editing; Chengyu Weng: Validation, Writing – review and editing; Yasong Wang:  
481 Visualization, Writing – review and editing; Mingxing Zhang: Investigation; Yunping Xu: Conceptualization, Writing – review  
482 and editing.

#### 483 **Competing Interests**

484 The authors declare that they have no conflict of interest.

#### 485 **Acknowledgments**

486 This work was supported by the National Natural Science Foundation of China (42206048). We would like to thank the captain,  
487 crew and especially all scientists of the R/V Songhang (Shanghai Ocean University) cruise for recovering the samples. Thank  
488 Xiaodi Lu and Yinwei Xi for the sampling and helping to measure XRF. Thank Xiaodi Lu for the assistance with lab analysis.  
489 Mike E. Meadows acknowledges financial support from the Jiangsu Provincial Government Overseas Talent 100 Plan,  
490 SBX2021010183.

#### 491 **Data Availability**

492 Data used in this study has been submitted in the Pangaea database (<https://www.pangaea.de>) with specific DOI:  
493 <https://doi.pangaea.de/10.1594/PANGAEA.987882> for pollen and spore, <https://doi.pangaea.de/10.1594/PANGAEA.987861>  
494 for organic-walled dinoflagellate cyst, and <https://doi.pangaea.de/10.1594/PANGAEA.987870> for microcharcoal.

#### 495 **References**

496 Aleman, J. C., Blarquez, O., Bentaleb, I., Bonté, P., Brossier, B., Carcaillet, C., Gond, V., Gourlet - Fleury, S., Kpolita, A.,  
497 Lefèvre, I., Oslisly, R., Power, M. J., Yongo, O. D., Bremond, L., and Favier, C.: Tracking land-cover changes with  
498 sedimentary charcoal in the Afrotropics. *Holocene*, 23, 1853–1862, doi: 10.1177/0959683613508159, 2013.  
499 An, Z.: The history and variability of the East Asian paleomonsoon climate. *Quat. Sci. Rev.*, 19(1), 171–187, doi: S0277-  
500 3791(99)00060-8, 2000.  
501 Andersen, K. K., Azuma, N., Barnola, J. M., Bigler, M., Biscaye, P., Caillon, N., Chappellaz, J., Clausen, H. B., Dahl-Jensen,  
502 D., Fischer, H., Flückiger, J., Fritzsche, D., Fujii, Y., Goto-Azuma, K., Grønsvold, K., Gundestrup, N. S., Hansson, M.,



503 Huber, C., Hvidberg, C. S., Johnsen, S. J., Jonsell, U., Jouzel, J., Kipfstuhl, S., Landais, A., Leuenberger, M., Lorrain, R.,  
504 Masson-Delmotte, V., Miller, H., Motoyama, H., Narita, H., Popp, T., Rasmussen, S. O., Raynaud, D., Rothlisberger, R.,  
505 Ruth, U., Samyn, D., Schwander, J., Shoji, H., Siggard-Andersen, M. L., Steffensen, J. P., Stocker, T., Sveinbjörnsdóttir, A. E.,  
506 Svensson, A., Takata, M., Tison, J. L., Thorsteinsson, T., Watanabe, O., Wilhelms, F., White, J. W. C., and North  
507 Greenland Ice Core Project, m.: High-resolution record of Northern Hemisphere climate extending into the last  
508 interglacial period. *Nature*, 431(7005), 147-151, doi: 10.1038/nature02805, 2004.

509 Bandara, G., Luo, C. X., Chen, C. X., Xiang, R., Herath, D. B., Yang, Z. J., and Thilakanayaka, V.: Sedimental pollen records  
510 in the northern South China Sea and their paleoenvironmental significance. *J. Asian Earth Sci.*, 241, Article 105457, doi:  
511 10.1016/j.jseas.2022.105457, 2023.

512 Barker, S., Greaves, M., and Elderfield, H.: A study of cleaning procedures used for foraminiferal Mg/Ca paleothermometry.  
513 *Geochem. Geophys. Geosyst.*, 4(9), doi: 10.1029/2003GC000559, 2003.

514 Blaauw, M., and Christen, J. A.: Flexible paleoclimate age-depth models using an autoregressive gamma process. *Bayesian  
515 Anal.*, 6(3), 457-474, 418, doi: 10.1214/11-BA618, 2011.

516 Cartapanis, O., Bianchi, D., Jaccard, S. L., and Galbraith, E. D.: Global pulses of organic carbon burial in deep-sea sediments  
517 during glacial maxima. *Nat. Commun.*, 7(1), 10796, doi: 10.1038/ncomms10796, 2016.

518 Chao, S., Shaw, P., and Wang, J.: Wind relaxation as possible cause of the South China Sea Warm Current. *J. Oceanogr.*,  
519 51(1), 111-132, doi: 10.1007/BF02235940, 1995.

520 Chen, C. A., and Huang, M.: A mid-depth front separating the South China Sea water and the Philippine sea water. *J. Oceanogr.*,  
521 52(1), 17-25, doi: 10.1007/BF02236530, 1996.

522 Chen, Y., Huang, E., Schefuß, E., Mohtadi, M., Steinke, S., Liu, J., Martínez-Méndez, G., and Tian, J.: Wetland expansion on  
523 the continental shelf of the northern South China Sea during deglacial sea level rise. *Quat. Sci. Rev.*, 231, 106202, doi:  
524 10.1016/j.quascirev.2020.106202, 2020.

525 Cheng, L., Abraham, J., Hausfather, Z., and Trenberth, K. E.: How fast are the oceans warming? *Science*, 363(6423), 128-129,  
526 doi: 10.1126/science.aav7619, 2019.

527 Cheng, Z., Wu, J., Luo, C., Liu, Z., Huang, E., Zhao, H., Dai, L., and Weng, C.: Coexistence of savanna and rainforest on the  
528 ice-age Sunda Shelf revealed by pollen records from southern South China Sea. *Quat. Sci. Rev.*, 301, 107947, doi:  
529 10.1016/j.quascirev.2022.107947, 2023.

530 Clift, P. D., Hodges, K. V., Heslop, D., Hannigan, R., Van Long, H., and Calves, G.: Correlation of Himalayan exhumation  
531 rates and Asian monsoon intensity. *Nat. Geosci.*, 1(12), 875-880, doi: 10.1038/ngeo351, 2008.

532 Conedera, M., Tinner, W., Neff, C., Meurer, M., Dickens, A. F., and Krebs, P.: Reconstructing past fire regimes: methods,  
533 applications, and relevance to fire management and conservation. *Quat. Sci. Rev.*, 28(5), 555-576, doi:  
534 10.1016/j.quascirev.2008.11.005, 2009.

535 Dai, L., and Weng, C.: A survey on pollen dispersal in the western Pacific Ocean and its paleoclimatological significance as a  
536 proxy for variation of the Asian winter monsoon. *Sci. China Earth Sci.*, 54(2), 249-258, doi: 10.1007/s11430-010-4027-  
537 7, 2011.

538 Dai, L., and Weng, C.: Marine palynological record for tropical climate variations since the late last glacial maximum in the  
539 northern South China Sea. *Deep-Sea. Res. Pt II*, 122, 153-162, doi: 10.1016/j.dsr2.2015.06.011, 2015.

540 Dai, L., Weng, C., and Mao, L.: Patterns of vegetation and climate change in the northern South China Sea during the last  
541 glaciation inferred from marine palynological records. *Palaeogeogr., Palaeoclimatol., Palaeoecol.*, 440, 249-258, doi:  
542 10.1016/j.palaeo.2015.08.041, 2015.

543 Dale, B.: Dinoflagellate cyst ecology: modeling and geological applications. In J. Jansonius and D. C. McGregor (Eds.),  
544 *Palynology: principles and applications* (Vol. 3, pp. 1249-1275). American Association of Stratigraphic Palynologists  
545 Foundation, 1996.

546 Ding, Z., Yu, Z., Rutter, N. W., and Liu, T.: Towards an orbital time scale for chinese loess deposits. *Quat. Sci. Rev.*, 13(1),  
547 39-70, doi: 10.1016/0277-3791(94)90124-4, 1994.

548 Fang, G., Fang, W. D., and Wang, K.: A survey of the study of the South China Sea upper ocean circulation. *Acta Oceanogr.  
549 Tai.*, 37, 1-16, 1998.

550 Felden, J., Möller, L., Schindler, U., Huber, R., Schumacher, S., Koppe, R., Diepenbroek, M., and Glöckner, F. O.: PANGAEA  
551 – Data Publisher for Earth & Environmental Science. *Sci. Data*, 10(1), 347, doi: 10.1038/s41597-023-02269-x, 2023.



552 Govin, A., Holzwarth, U., Heslop, D., Ford Keeling, L., Zabel, M., Mulitza, S., Collins, J. A., and Chiessi, C. M.: Distribution  
553 of major elements in Atlantic surface sediments (36°N–49°S): Imprint of terrigenous input and continental weathering.  
554 *Geochem. Geophys. Geosyst.*, 13(1), doi: 10.1029/2011GC003785, 2012.

555 Grimm, E.: Tilia and TGVView 19 version 2.0. 41. software. Springfield, USA: Illinois State Museum, Research and Collection  
556 Center, 2015.

557 Hanebuth, T., Stattegger, K., and Grootes, P. M.: Rapid flooding of the Sunda Shelf: A late-glacial sea-level record. *Science*,  
558 288(5468), 1033–1035, doi: 10.1126/science.288.5468.1033, 2000.

559 Haynes, J. R.: Foraminifera. Palgrave Macmillan London, doi: 10.1007/978-1-349-05397-1, 1981.

560 Holzwarth, U., Esper, O., and Zonneveld, K.: Distribution of organic-walled dinoflagellate cysts in shelf surface sediments of  
561 the Benguela upwelling system in relationship to environmental conditions. *Mar. Micropaleontol.*, 64(1–2), 91–119, doi:  
562 10.1016/j.marmicro.2007.04.001, 2007.

563 Hu, D., Clift, P. D., Böning, P., Hannigan, R., Hillier, S., Blusztajn, J., Wan, S., and Fuller, D. Q.: Holocene evolution in  
564 weathering and erosion patterns in the Pearl River delta. *Geochem. Geophys. Geosyst.*, 14(7), 2349–2368, doi:  
565 10.1002/ggge.20166, 2013.

566 Hu, J., Kawamura, H., Hong, H., and Qi, Y.: A review on the currents in the South China Sea: Seasonal circulation, South  
567 China Sea warm current and Kuroshio intrusion. *J. Oceanogr.*, 56(6), 607–624, doi: 10.1023/A:1011117531252, 2000.

568 Huang, C., Wu, L., Cheng, J., Qu, X., Luo, Y., Zhang, H., Ye, F., and Wei, G.: Sedimentary responses to climatic variations  
569 and Kuroshio intrusion into the northern South China Sea since the last deglaciation. *Global Planet. Change*, 245, 104671,  
570 doi: 10.1016/j.gloplacha.2024.104671, 2025.

571 Huang, K., You, C., Lin, H., and Shieh, Y.: In situ calibration of Mg/Ca ratio in planktonic foraminiferal shell using time series  
572 sediment trap: A case study of intense dissolution artifact in the South China Sea. *Geochem. Geophys. Geosyst.*, 9(4),  
573 doi: 10.1029/2007GC001660, 2008.

574 Hughen, K. A., Baillie, M. G. L., Bard, E., Warren Beck, J., Bertrand, C. J. H., Blackwell, P. G., Buck, C. E., Burr, G. S.,  
575 Cutler, K. B., Damon, P. E., Edwards, R. L., Fairbanks, R. G., Friedrich, M., Guilderson, T. P., Kromer, B., McCormac,  
576 G., Manning, S., Bronk Ramsey, C., Reimer, P. J., Reimer, R. W., Remmele, S., Southon, J. R., Stuiver, M., Talamo, S.,  
577 Taylor, F. W., Van der Plicht, J., and Weyhenmeyer, C. E.: Marine04 marine radiocarbon age calibration, 0–26 cal kyr  
578 BP. *Radiocarbon*, 46(3), 1059–1086, doi: 10.1017/S003382200033002, 2004.

579 Jiwarungreangkul, T., and Liu, Z.: East Asian monsoon and sea-level controls on clay mineral variations in the southern  
580 South China Sea since the Last Glacial Maximum. *Quat. Int.*, 592, 1–11, doi: 10.1016/j.quaint.2021.04.033, 2021.

581 Kaars, S. v. d., Wang, X., Kershaw, P., Guichard, F., and Setiabudi, D. A.: A Late Quaternary palaeoecological record from  
582 the Banda Sea, Indonesia: patterns of vegetation, climate and biomass burning in Indonesia and northern Australia.  
583 *Palaeogeogr., Palaeoclimatol., Palaeoecol.*, 155(1), 135–153, doi: 10.1016/S0031-0182(99)00098-X, 2000.

584 Kissel, C., Laj, C., Jian, Z., Wang, P., Wandres, C., and Rebolledo-Vieyra, M.: Past environmental and circulation changes in  
585 the South China Sea: Input from the magnetic properties of deep-sea sediments. *Quat. Sci. Rev.*, 236, 106263, doi:  
586 10.1016/j.quascirev.2020.106263, 2020.

587 Lambeck, K., Rouby, H., Purcell, A., Sun, Y., and Cambridge, M.: Sea level and global ice volumes from the Last Glacial  
588 Maximum to the Holocene. *Proc. Natl. Acad. Sci. U. S. A.*, 111(43), 15296–15303, doi: 10.1073/pnas.1411762111, 2014.

589 Laskar, J., Robutel, P., Joutel, F., Gastineau, M., Correia, A. C. M., and Levrard, B.: A long-term numerical solution for the  
590 insolation quantities of the Earth. *Astronomy & Astrophysics*, 428, 261–285, doi: 10.1051/0004-6361:20041335, 2004.

591 Lee, C. M., van Geel, B., and Gosling, W. D.: On the use of spores of coprophilous fungi preserved in sediments to indicate  
592 past herbivore presence. *Quaternary*, 5(3), 30, doi: 10.3390/quat5030030, 2022.

593 Li, C., Li, Y., Zheng, Y., Yu, S., Tang, L., Li, B., and Cui, Q.: A high-resolution pollen record from East China reveals large  
594 climate variability near the Northgrippian-Meghalayan boundary (around 42 years ago) exerted societal influence.  
595 *Palaeogeogr., Palaeoclimatol., Palaeoecol.*, 512, 156–165, doi: 10.1016/j.palaeo.2018.07.031, 2018a.

596 Li, L., Wang, H., Luo, B., and He, J.: The characterizations and paleoceanographic significances of organic and inorganic  
597 carbon in northern South China Sea during past 40 ka. *Mar. Geol. & Qua. Geol.*, 28(6), 79–85, doi:  
598 10.3724/sp.J.1140.2008.06079, 2008.

599 Li, M., Ouyang, T., Tian, C., Zhu, Z., Peng, S., Tang, Z., Qiu, Y., Zhong, H., and Peng, X.: Sedimentary responses to the East  
600 Asian monsoon and sea level variations recorded in the northern South China Sea over the past 3 kyr. *J. Asian Earth Sci.*,  
601 171, 213–224, doi: 10.1016/j.jseas.2018.01.001, 2019.



602 Li, Z., Pospelova, V., Kawamura, H., Luo, C., Mertens, K. N., Hernández-Almeida, I., Yin, K., Wu, Y., Wu, H., and Xiang, R.: Dinoflagellate cyst distribution in surface sediments from the South China Sea in relation to hydrographic conditions  
603 and primary productivity. *Mar. Micropaleontol.*, 159, 101815, doi: 10.1016/j.marmicro.2019.101815, 2020.

604 Li, Z., Pospelova, V., Lin, H.-L., Liu, L., Song, B., and Gong, W.: Seasonal dinoflagellate cyst production and terrestrial  
605 palynomorph deposition in the East Asian Monsoon influenced South China Sea: A sediment trap study from the  
606 Southwest Taiwan waters. *Rev. Palaeobot. Palynol.*, 257, 117-139, doi: 10.1016/j.revpalbo.2018.07.007, 2018b.

607 Li, Z., Pospelova, V., Liu, L., Francois, R., Wu, Y., Mertens, K. N., Saito, Y., Zhou, R., Song, B., and Xie, X.: High-resolution  
608 reconstructions of Holocene sea-surface conditions from dinoflagellate cyst assemblages in the northern South China Sea.  
609 *Mar. Geol.*, 438, 106528, doi: 10.1016/j.margeo.2021.106528, 2021.

610 Li, Z., Pospelova, V., Liu, L., Zhou, R., and Song, B.: High-resolution palynological record of Holocene climatic and  
611 oceanographic changes in the northern South China Sea. *Palaeogeogr., Palaeoclimatol., Palaeoecol.*, 483, 94-124, doi:  
612 10.1016/j.palaeo.2017.03.009, 2017.

613 Li, Z., Pospelova, V., Mertens, K. N., Liu, L., Wu, Y., Li, C., and Gu, H.: Evaluation of organic-walled dinoflagellate cyst  
614 distributions in coastal surface sediments of the China Seas in relation with hydrographic conditions for  
615 paleoceanographic reconstruction. *Quat. Int.*, 661, 60-75, doi: 10.1016/j.quaint.2023.03.007, 2023.

616 Lin, D., Chen, M., Yamamoto, M., and Yokoyama, Y.: Millennial-scale alkenone sea surface temperature changes in the  
617 northern South China Sea during the past 45,000 years (MD972146). *Quat. Int.*, 333, 207-215, doi:  
618 10.1016/j.quaint.2014.03.062, 2014.

619 Liu, J., Xiang, R., Chen, Z., Chen, M., Yan, W., Zhang, L., and Chen, H.: Sources, transport and deposition of surface  
620 sediments from the South China Sea. *Deep Sea Res. (I Oceanogr. Res. Pap.)*, 71, 92-102, doi: 10.1016/j.dsr.2012.09.006,  
621 2013.

622 Liu, J., Xiang, R., Kao, S. J., Fu, S., and Zhou, L.: Sedimentary responses to sea-level rise and Kuroshio Current intrusion  
623 since the Last Glacial Maximum: Grain size and clay mineral evidence from the northern South China Sea slope.  
624 *Palaeogeogr., Palaeoclimatol., Palaeoecol.*, 450, 111-121, doi: 10.1016/j.palaeo.2016.03.002, 2016a.

625 Liu, K., Chao, S., Shaw, P., Gong, G., Chen, C., and Tang, T.: Monsoon-forced chlorophyll distribution and primary production  
626 in the South China Sea: observations and a numerical study. *Deep Sea Res. (I Oceanogr. Res. Pap.)*, 49(8), 1387-1412,  
627 doi: 10.1016/S0967-0637(02)00035-3, 2002.

628 Liu, L., Guan, H., Feng, J., Xu, L., Mao, S., and Liu, L.: Composition of glycerol dibiphytanyl glycerol tetraethers (GDGTs)  
629 and its responses to paleotemperature and monsoon changes since 31ka in northern South China Sea. *Mar. Geol. & Qua.*  
630 *Geol.*, 40(3), 144-159, doi: 10.16562/j.cnki.0256-1492.2020021101, 2020.

631 Liu, Z., Colin, C., Li, X., Zhao, Y., Tuo, S., Chen, Z., Siringan, F. P., Liu, J. T., Huang, C.-Y., You, C.-F., and Huang, K.-F.:  
632 Clay mineral distribution in surface sediments of the northeastern South China Sea and surrounding fluvial drainage  
633 basins: Source and transport. *Mar. Geol.*, 277(1), 48-60, doi: 10.1016/j.margeo.2010.08.010, 2010.

634 Liu, Z., Trentesaux, A., Clemens, S. C., Colin, C., Wang, P., Huang, B., and Boulay, S.: Clay mineral assemblages in the  
635 northern South China Sea: implications for East Asian monsoon evolution over the past 2 million years. *Mar. Geol.*,  
636 201(1), 133-146, doi: 10.1016/S0025-3227(03)00213-5, 2003.

637 Liu, Z., Zhao, Y., Colin, C., Stattegger, K., Wiesner, M. G., Huh, C., Zhang, Y., Li, X., Sompongchaiyakul, P., You, C., Huang,  
638 C., Liu, J. T., Siringan, F. P., Le, K. P., Sathiamurthy, E., Hantoro, W. S., Liu, J., Tuo, S., Zhao, S., Zhou, S., He, Z.,  
639 Wang, Y., Bunsomboonsakul, S., and Li, Y.: Source-to-sink transport processes of fluvial sediments in the South China  
640 Sea. *Earth-Sci. Rev.*, 153, 238-273, doi: 10.1016/j.earscirev.2015.08.005, 2016b.

641 Luo, C., Chen, C., Xiang, R., Jiang, W., Liu, J., Lu, J., Su, X., Zhang, Q., Yang, Y., and Yang, M.: Study of modern pollen  
642 distribution in the northeastern Indian Ocean and their application to paleoenvironment reconstruction. *Rev. Palaeobot.*  
643 *Palynol.*, 256, 50-62, doi: 10.1016/j.revpalbo.2018.05.007, 2018.

644 Luo, C., Chen, M., Xiang, R., Liu, J., Zhang, L., and Lu, J.: Comparison of modern pollen distribution between the northern  
645 and southern parts of the South China Sea. *Int. J. Biometeorol.*, 59(4), 397-415, doi: 10.1007/s00484-014-0852-2, 2015.

646 Luo, C., Jiang, C., Yang, M., Chen, M., Xiang, R., Zhang, L., Liu, J., and Pan, A.: Transportation modes of pollen in surface  
647 waters in the South China Sea and their environmental significance. *Rev. Palaeobot. Palynol.*, 225, 95-105, doi:  
648 10.1016/j.revpalbo.2015.11.004, 2016.

649 Luo, Y., and Sun, X.: Vegetation evolution and millennial-scale climatic fluctuations since Last Glacial Maximum in pollen  
650 record from northern South China Sea. *Chin. Sci. Bull.*, 50(8), 793-799, doi: 10.1007/BF03183681, 2005.



652 Luo, Y., and Sun, X.: Vegetation evolution and its response to climatic change during 3.15–0.67 Ma in deep-sea pollen record  
653 from northern South China Sea. *Chin. Sci. Bull.*, 58(3), 364–372, doi: 10.1007/s11434-012-5374-x, 2013.

654 Marret, F., and Zonneveld, K. A. F.: Atlas of modern organic-walled dinoflagellate cyst distribution. *Rev. Palaeobot. Palynol.*,  
655 125(1–2), 1–200, doi: 10.1016/S0034-6667(02)00229-4, 2003.

656 Matsuoka, K.: Dinoflagellate cysts and pollen in pelagic sediments of the northern part of the Philippin Sea. *Bull., Faculty of  
657 Liberal Arts, Nagasaki University. (Natural Science)*, 21(2), 59–70, 1981.

658 Milliman, J. D., and Syvitski, J. P. M.: Geomorphic/tectonic control of sediment discharge to the ocean: The importance of  
659 small mountainous rivers. *J. Geol.*, 100(5), 525–544, doi: 10.1086/629606, 1992.

660 Mooney, S. D., and Tinner, W.: The analysis of charcoal in peat and organic sediments. *Mires Peat*, 7(09), doi:  
661 10.19189/001c.128417, 2011.

662 Oppo, D. W., and Sun, Y.: Amplitude and timing of sea-surface temperature change in the northern South China Sea: Dynamic  
663 link to the East Asian monsoon. *Geology*, 33(10), 785–788, doi: 10.1130/G21867.1, 2005.

664 Schönfeld, J., Alve, E., Geslin, E., Jorissen, F., Korsun, S., and Spezzaferri, S.: The FOBIMO (FOraminiferal BIo-MOnitoring)  
665 initiative—Towards a standardised protocol for soft-bottom benthic foraminiferal monitoring studies. *Mar.  
666 Micropaleontol.*, 94–95, 1–13, doi: 10.1016/j.marmicro.2012.06.001, 2012.

667 Smayda, T. J., and Trainer, V. L.: Dinoflagellate blooms in upwelling systems: Seeding, variability, and contrasts with diatom  
668 bloom behaviour. *Prog. Oceanogr.*, 85(1), 92–107, doi: 10.1016/j.pocean.2010.02.006, 2010.

669 Stibig, H.-J., Belward, A. S., Roy, P. S., Rosalina-Wasrin, U., Agrawal, S., Joshi, P. K., Beuchle, R., Fritz, S., Mubareka, S.,  
670 and Giri, C.: A land-cover map for South and Southeast Asia derived from SPOT-VEGETATION data. *J. Biogeogr.*,  
671 34(4), 625–637, doi: 10.1111/j.1365-2699.2006.01637.x, 2007.

672 Stuiver, M., and Reimer, P. J.: Extended 14C Data Base and Revised CALIB 3.0 14C Age Calibration Program. *Radiocarbon*,  
673 35(1), 215–230, doi: 10.1017/S0033822200013904, 1993.

674 Sun, X., Li, X., and Beug, H.-J.: Pollen distribution in hemipelagic surface sediments of the South China Sea and its relation  
675 to modern vegetation distribution. *Mar. Geol.*, 156(1), 211–226, doi: 10.1016/S0025-3227(98)00180-7, 1999.

676 Sun, X., Li, X., and Chen, H.: Evidence for natural fire and climate history since 37 ka BP in the northern part of the South  
677 China Sea. *Sci. China Ser. D-Earth Sci.*, 43(5), 487–493, doi: 10.1007/bf02875310, 2000a.

678 Sun, X., Li, X., Luo, Y., and Chen, X.: The vegetation and climate at the last glaciation on the emerged continental shelf of  
679 the South China Sea. *Palaeogeogr., Palaeoclimatol., Palaeoecol.*, 160(3), 301–316, doi: 10.1016/S0031-0182(00)00078-  
680 X, 2000b.

681 Sun, X., and Luo, Y.: Pollen record of the last 280 ka from deep sea sediments of the northern South China Sea. *Sci. China  
682 Ser. D-Earth Sci.*, 44(10), 879–888, doi: 10.1007/BF02907079, 2001.

683 Sun, X., Luo, Y., Huang, F., Tian, J., and Wang, P.: Deep-sea pollen from the South China Sea: Pleistocene indicators of East  
684 Asian monsoon. *Mar. Geol.*, 201(1), 97–118, doi: 10.1016/S0025-3227(03)00211-1, 2003.

685 Tang, L., Mao, L., Shu, J., Li, C., Shen, C., and Zhou, Z.: *Atlas of Quaternary pollen and spores in China*. Science Press and  
686 Springer Nature Singapore Pte Ltd, doi: 10.1007/978-981-13-7103-5, 2020.

687 ter Braak, C. J. F., and Smilauer, P.: *Canoco reference manual and user's guide: software for ordination, version 5.0.*  
688 Microcomputer Power, Ithaca, NY, USA. 2012.

689 Tian, J., Huang, E., and Pak, D. K.: East Asian winter monsoon variability over the last glacial cycle: Insights from a latitudinal  
690 sea-surface temperature gradient across the South China Sea. *Palaeogeogr., Palaeoclimatol., Palaeoecol.*, 292(1–2), 319–  
691 324, doi: 10.1016/j.palaeo.2010.04.005, 2010.

692 Tian, J., Wang, P. X., and Cheng, X. R.: Responses of foraminiferal isotopic variations at ODP Site 1143 in the southern South  
693 China Sea to orbital forcing. *Sci. China Ser. D-Earth Sci.*, 47(10), 943–953, doi: 10.1360/03yd0129, 2004.

694 Tian, J., Xie, X., Ma, W., Jin, H., and Wang, P.: X-ray fluorescence core scanning records of chemical weathering and monsoon  
695 evolution over the past 5 Myr in the southern South China Sea. *Paleoceanography*, 26(4), doi: 10.1029/2010PA002045,  
696 2011.

697 Tyszka, J., Godos, K., Goleń, J., and Radmacher, W.: Foraminiferal organic linings: Functional and phylogenetic challenges.  
698 *Earth-Sci. Rev.*, 220, 103726, doi: 10.1016/j.earscirev.2021.103726, 2021.

699 Wan, S., and Jian, Z.: Deep water exchanges between the South China Sea and the Pacific since the last glacial period.  
700 *Paleoceanography*, 29(12), 1162–1178, doi: 10.1002/2013PA002578, 2014.



701 Wan, S., Li, A., Clift, P. D., and Stuut, J.-B. W.: Development of the East Asian monsoon: Mineralogical and sedimentologic  
702 records in the northern South China Sea since 20 Ma. *Palaeogeogr., Palaeoclimatol., Palaeoecol.*, 254(3), 561-582, doi:  
703 10.1016/j.palaeo.2007.07.009, 2007.

704 Wang, C.: The forests of China. Maria Moors Cabot Foundation No.5. Harvard University, Cambridge Mass, USA, 717, 1961.

705 Wang, L., Sarnthein, M., Erlenkeuser, H., Grootes, P. M., Grimalt, J. O., Pelejero, C., and Linck, G.: Holocene variations in  
706 Asian monsoon moisture: A bidecadal sediment record from the South China Sea. *Geophys. Res. Lett.*, 26(18), 2889-  
707 2892, doi: 10.1029/1999GL900443, 1999.

708 Wang, P., Li, Q., and Tian, J.: Pleistocene paleoceanography of the South China Sea: Progress over the past 20 years. *Mar.*  
709 *Geol.*, 352, 381-396, doi: 10.1016/j.margeo.2014.03.003, 2014.

710 Wang, P., and Sun, X.: Last glacial maximum in China: comparison between land and sea. *Catena*, 23(3), 341-353, doi:  
711 10.1016/0341-8162(94)90077-9, 1994.

712 Wang, P., Wang, B., Cheng, H., Fasullo, J., Guo, Z., Kiefer, T., and Liu, Z.: The global monsoon across time scales:  
713 Mechanisms and outstanding issues. *Earth-Sci. Rev.*, 174, 84-121, doi: 10.1016/j.earscirev.2017.07.006, 2017.

714 Wang, X., Sun, X., Wang, P., and Stattegger, K.: Vegetation on the Sunda Shelf, South China Sea, during the Last Glacial  
715 Maximum. *Palaeogeogr., Palaeoclimatol., Palaeoecol.*, 278(1), 88-97, doi: 10.1016/j.palaeo.2009.04.008, 2009.

716 Wang, Y. J., Cheng, H., Edwards, R. L., An, Z. S., Wu, J. Y., Shen, C.-C., and Dorale, J. A.: A high-resolution absolute-dated  
717 late Pleistocene monsoon record from Hulu Cave, China. *Science*, 294(5550), 2345-2348, doi: 10.1126/science.1064618,  
718 2001.

719 Wei, G., Liu, Y., Li, X., Shao, L., and Fang, D.: Major and trace element variations of the sediments at ODP Site 1144, South  
720 China Sea, during the last 230 ka and their paleoclimate implications. *Palaeogeogr., Palaeoclimatol., Palaeoecol.*, 212(3),  
721 331-342, doi: 10.1016/j.palaeo.2004.06.011, 2004.

722 Whitmore, T. C.: Rain forests: Tropical rain forests of the far east. *Science*, 228(4701), 874-875, doi:  
723 10.1126/science.228.4701.874, 1985.

724 Williams, G., Fensome, R., and MacRae, R.: DINOFLAJ3, 2017.

725 Xie, S.-P., Deser, C., Vecchi, G. A., Ma, J., Teng, H., and Wittenberg, A. T.: Global Warming Pattern Formation: Sea Surface  
726 Temperature and Rainfall. *J. Clim.*, 23(4), 966-986, doi: 10.1175/2009JCLI3329.1, 2010.

727 Xie, X., Zheng, H.-B., and Qiao, P.-J.: Millennial climate changes since MIS 3 revealed by element records in deep-sea  
728 sediments from northern South China Sea. *Chin. Sci. Bull.*, 59(8), 776-784, doi: 10.1007/s11434-014-0117-9, 2014.

729 Yu, S., Zheng, Z., Chen, F., Jing, X., Kershaw, P., Moss, P., Peng, X., Zhang, X., Chen, C., Zhou, Y., Huang, K., and Gan, H.:  
730 A last glacial and deglacial pollen record from the northern South China Sea: New insight into coastal-shelf  
731 paleoenvironment. *Quat. Sci. Rev.*, 157, 114-128, doi: 10.1016/j.quascirev.2016.12.012, 2017.

732 Yuan, D., Cheng, H., Edwards, R. L., Dykoski, C. A., Kelly, M. J., Zhang, M., Qing, J., Lin, Y., Wang, Y., Wu, J., Dorale, J.  
733 A., An, Z., and Cai, Y.: Timing, duration, and transitions of the last interglacial asian monsoon. *Science*, 304(5670), 575-  
734 578, doi: 10.1126/science.1091220, 2004a.

735 Yuan, Y. C., Bu, X. W., Liao, G. H., Lou, R. Y., Su, J. L., and Wang, K. S.: Diagnostic calculation of the upper-layer circulation  
736 in the South China Sea during the winter of 1998. *Acta Oceanol. Sin.*, 23(2), 187-199, 2004b.

737 Zhang, H., Liu, C., Jin, X., Shi, J., Zhao, S., and Jian, Z.: Dynamics of primary productivity in the northern South China Sea  
738 over the past 24,000 years. *Geochem. Geophys. Geosyst.*, 17(12), 4878-4891, doi: 10.1002/2016GC006602, 2016.

739 Zhao, X., Dupont, L., Schefuß, E., Bouimetarhan, I., and Wefer, G.: Palynological evidence for Holocene climatic and  
740 oceanographic changes off western South Africa. *Quat. Sci. Rev.*, 165, 88-101, doi: 10.1016/j.quascirev.2017.04.022,  
741 2017.

742 Zheng, Z., and Lei, Z. Q.: A 400,000 year record of vegetational and climatic changes from a volcanic basin, Leizhou Peninsula,  
743 southern China. *Palaeogeogr., Palaeoclimatol., Palaeoecol.*, 145(4), 339-362, doi: 10.1016/S0031-0182(98)00107-2,  
744 1999.

745 Zhong, Y., Chen, Z., Li, L., Liu, J., Li, G., Zheng, X., Wang, S., and Mo, A.: Bottom water hydrodynamic provinces and  
746 transport patterns of the northern South China Sea: Evidence from grain size of the terrigenous sediments. *Cont. Shelf  
747 Res.*, 140, 11-26, doi: 10.1016/j.csr.2017.01.023, 2017.

748 Zhou, B., Zheng, H., Yang, W., Taylor, D., Lu, Y., Wei, G., Li, L., and Wang, H.: Climate and vegetation variations since the  
749 LGM recorded by biomarkers from a sediment core in the northern South China Sea. *J. Quat. Sci.*, 27(9), 948-955, doi:  
750 10.1002/jqs.2588, 2012.



751 Zonneveld, K. A. F., Harper, K., Klügel, A., Chen, L., De Lange, G., and Versteegh, G. J. M.: Climate change, society, and  
752 pandemic disease in Roman Italy between 200 BCE and 600 CE. *Sci. Adv.*, 10(4), eadk1033, doi: 10.1126/sciadv.adk1033,  
753 2024.

754 Zonneveld, K. A. F., Marret, F., Versteegh, G. J. M., Bogus, K., Bonnet, S., Bouimetarhan, I., Crouch, E., de Vernal, A.,  
755 Elshanawany, R., Edwards, L., Esper, O., Forke, S., Grøsfjeld, K., Henry, M., Holzwarth, U., Kiel, J. F., Kim, S.,  
756 Ladouceur, S., Ledu, D., Chen, L., Limoges, A., Londeix, L., Lu, S. H., Mahmoud, M. S., Marino, G., Matsouka, K.,  
757 Matthiessen, J., Mildenhall, D. C., Mudie, P., Neil, H. L., Pospelova, V., Qi, Y., Radi, T., Richerol, T., Rochon, A.,  
758 Sangiorgi, F., Solignac, S., Turon, J. L., Verleye, T., Wang, Y., Wang, Z., and Young, M.: Atlas of modern dinoflagellate  
759 cyst distribution based on 2405 data points. *Rev. Palaeobot. Palynol.*, 191(0), 1-197, doi: 10.1016/j.revpalbo.2012.08.003,  
760 2013.

761 Zonneveld, K. A. F., and Pospelova, V.: A determination key for modern dinoflagellate cysts. *Palynology*, 39(3), 387-409, doi:  
762 10.1080/01916122.2014.990115, 2015.

763 Zonneveld, K. A. F., Versteegh, G., and Kodrans-Nsiah, M.: Preservation and organic chemistry of Late Cenozoic organic-  
764 walled dinoflagellate cysts: A review. *Mar. Micropaleontol.*, 68(1-2), 179-197, doi: 10.1016/j.marmicro.2008.01.015,  
765 2008.